sid.inpe.br/mtc-m21d/2021/06.29.11.45-TDI

STUDY OF THE MAXIMUM USABLE FREQUENCY DURING THE SAINT PATRICK'S DAY GEOMAGNETIC STORM AT THE BRAZILIAN SECTOR

Nwankwo Onyinye Gift

Master's Dissertation of the Graduate Course in Space Geophysics, guided by Drs. Cláudia Maria Nicoli Cândido, and Fábio Becker Guedes, approved in June 04, 2021.

URL of the original document:
<http://urlib.net/8JMKD3MGP3W34T/44UM49L>

INPE
São José dos Campos
2021

PUBLISHED BY:

Instituto Nacional de Pesquisas Espaciais - INPE
Coordenação de Ensino, Pesquisa e Extensão (COEPE)
Divisão de Biblioteca (DIBIB)
CEP 12.227-010
São José dos Campos - SP - Brasil
Tel.:(012) 3208-6923/7348
E-mail: pubtc@inpe.br

DIGITAL LIBRARY:
Dr. Gerald Jean Francis Banon
Clayton Martins Pereira - Divisão de Biblioteca (DIBIB)
DOCUMENT REVIEW:
Simone Angélica Del Ducca Barbedo - Divisão de Biblioteca (DIBIB)
André Luis Dias Fernandes - Divisão de Biblioteca (DIBIB)
ELECTRONIC EDITING:
Ivone Martins - Divisão de Biblioteca (DIBIB)
André Luis Dias Fernandes - Divisão de Biblioteca (DIBIB)

sid.inpe.br/mtc-m21d/2021/06.29.11.45-TDI

STUDY OF THE MAXIMUM USABLE FREQUENCY DURING THE SAINT PATRICK'S DAY GEOMAGNETIC STORM AT THE BRAZILIAN SECTOR

Nwankwo Onyinye Gift

Master's Dissertation of the Graduate Course in Space Geophysics, guided by Drs. Cláudia Maria Nicoli Cândido, and Fábio Becker Guedes, approved in June 04, 2021.

URL of the original document:
<http://urlib.net/8JMKD3MGP3W34T/44UM49L>

INPE
São José dos Campos
2021

Cataloging in Publication Data

Gift, Nwankwo Onyinye.

G366s Study of the maximum usable frequency during the Saint Patrick's day geomagnetic storm at the brazilian sector / Nwankwo Onyinye Gift. – São José dos Campos : INPE, 2021.

xxiv + 80 p. ; (sid.inpe.br/mtc-m21d/2021/06.29.11.45-TDI)

Dissertation (Master in Space Geophysics) – Instituto Nacional de Pesquisas Espaciais, São José dos Campos, 2021.

Guiding : Drs. Cláudia Maria Nicoli Cândido, and Fábio Becker Guedes.

1. Ionosphere. 2. Ionospheric parameters. 3. Geomagnetic disturbances. 4. Radio communication. 5. Maximum Usable Frequency (MUF). I.Title.

CDU 550.388

MINISTÉRIO DA
CIÊNCIA, TECNOLOGIA
E INOVAÇÕES

INSTITUTO NACIONAL DE PESQUISAS ESPACIAIS

DEFESA FINAL DE DISSERTAÇÃO DE NWANKWO ONYINYE GIFT
BANCA Nº 173/2021, REG 81990/2019

No dia 04 de junho de 2021, às 09h00min, por Vídeo Conferência, o(a) aluno(a) mencionado(a) acima defendeu seu trabalho final (apresentação oral seguida de arguição) perante uma Banca Examinadora, cujos membros estão listados abaixo. O(A) aluno(a) foi APROVADO(A) pela Banca Examinadora por unanimidade, em cumprimento ao requisito exigido para obtenção do Título de Mestra em Geofísica Espacial / Ciências Atmosféricas . O trabalho precisa da incorporação das correções sugeridas pela Banca Examinadora e revisão final pelo(s) orientador(es).

Novo Título: "STUDY OF THE MAXIMUM USABLE FREQUENCY DURING THE SAINT PATRICK'S DAY GEOMAGNETIC STORM AT THE BRAZILIAN SECTOR"

Membros da Banca

Dr. Marlos Rockenbach da Silva - Presidente - INPE
Dra. Cláudia Maria Nicoli Cândido - Orientadora – INPE
Dr. Fábio Becker Guedes – Orientador - INPE
Dr. Jonas Rodrigues de Souza - Membro Interno - INPE
Dr. Renato Alves Borges - Membro Externo – UnB

---

sei! assinatura eletrônica

Documento assinado eletronicamente por **Fábio Becker Guedes**, **Pesquisador**, em 21/09/2021, às 16:03 (horário oficial de Brasília), com fundamento no § 3º do art. 4º do Decreto nº 10.543, de 13 de novembro de 2020.

---

sei! assinatura eletrônica

Documento assinado eletronicamente por **Marlos Rockenbach da Silva**, **Pesquisador**, em 21/09/2021, às 16:36 (horário oficial de Brasília), com fundamento no § 3º do art. 4º do Decreto nº 10.543, de 13 de novembro de 2020.

---

sei! assinatura eletrônica

Documento assinado eletronicamente por **Jonas Rodrigues de Souza**, **Pesquisador**, em 21/09/2021, às 17:04 (horário oficial de Brasília), com fundamento no § 3º do art. 4º do Decreto nº 10.543, de 13 de novembro de 2020.

---

sei! assinatura eletrônica

Documento assinado eletronicamente por **CLAUDIA MARIA NICOLI CANDIDO (E)**, **Usuário Externo**, em 22/09/2021, às 09:11 (horário oficial de Brasília), com fundamento no § 3º do art. 4º do Decreto nº 10.543, de 13 de novembro de 2020.

---

sei! assinatura eletrônica

Documento assinado eletronicamente por **Renato Alves Borges (E)**, **Usuário Externo**, em 30/09/2021, às 19:36 (horário oficial de Brasília), com fundamento no § 3º do art. 4º do Decreto nº 10.543, de 13 de novembro de 2020.

"Making your mark on the world is hard. If it were easy, everybody would do it. But it's not! It takes patience, it takes commitment, and it comes with plenty of failure along the way. The real test is not whether you avoid this failure, it's whether you let it harden or shame you into inaction, or whether you learn from it; whether you choose to persevere."

Barack Obama

I dedicate this research dissertation to my sweet parents ***John & Cecilia Nwankwo****, also, to the memory of my late sister* ***Miss Charity Nwankwo****.*

ACKNOWLEDGEMENTS

I am eternally grateful to God Almighty for his unconditional love and unending blessings towards me, my career and academics.

I would like to thank my amazing parents, Elder & Deaconess John Nwankwo, whose prayers and subtle words of affection keeps me going. Thank you Mom and Dad for grounding me in Prayers and the Fear of God. I also appreciate my siblings, most especially Dr. Patrick Chukwudi Nwankwo, Mr Anayo Nwankwo, and Mrs Tivkor Nkiruka for their regular talks and chats, deep insights and moral support. Even my little nieces and nephews (David, Kelvin, Success, Henrietta, Vanessa, Josiah, Melvin, Brian, Chizaram, Jaden and Irvin). I can't tell you all how much you have been my source of stability and purpose.

I am filled with gratitude to the National Institute for Space Research (INPE) together with the agency that promotes this research, CNPq. I wish to show my sincere appreciation to my advisors, Dr. Fabio Guedes-Becker and Dr. Claudia Nicoli Candido, for their guidance through this research project. Also, I thank all the Professors in the department of Space Geophysics who contributed to my knowledge.

I wish to acknowledge and appreciate the Director/CE of Centre for Atmospheric Research, National Space Research Development Agency (CAR-NASRDA), Professor Babatunde Rabiu, for his mentorship and fatherly role in my career. Also, I truly appreciate the Coordinator Dr. Daniel Okoh and entire staff of Space Environment Research Laboratory, Centre for Atmospheric Research (SERL-CAR). My heartfelt appreciation goes to the following institutions for facilitating my Masters study leave letter at INPE: Center of Atmospheric Research; National Space Research and Development Agency; Federal Ministry of Science, Technology Innovation; and Federal Republic of Nigeria.

I am thankful to the members of the examination board for having accepted the invitation to evaluate this work and for all the suggestions and remarks.

I truly appreciate all my friends (Amadi Brians Chinonso, Alabi Bukola Elizabeth, Zion Pibowei, Oyekunle John, Dauda Kashim and Obielo Prisca) for how they continually kept in touch with me, even with the long distance. The conversations they make brought me calm during this project, even amidst the global pandemic chaos.

Finally, to my colleagues; Samuel, Stella, Taiwo, Mr. Tunde and Frank, I appreciate you all for the support during the disciplines, discussions and help with theory.

ABSTRACT

This work presents a study of the Maximum Usable Frequency, MUF, variation during the first super geomagnetic storm of solar cycle 24, on March 17^{th}, 2015, referred to as Saint Patrick's Day Storm. For this purpose, ionospheric parameters such as the plasma critical frequency, foF2, the F-layer's virtual and peak heights, h'F and hmF2, respectively, and the Maximum Usable Frequency, MUF extracted from Digisondes were analyzed. Ionospheric data were taken from ground-based Digisondes installed at two representative regions in Brazil: equatorial region, over São Luis, MA (2.5^{o}S, 44.3^{o}W, dip angle 5^{o}S) and the low-latitude region around the southern crest of EIA, at Campo Grande, MT (20.44^{o}S, 54.65^{o}W, dip angle 22.3^{o}S). The ionospheric parameter MUF is of great importance for HF radio communication, and strongly depends on the ionospheric plasma density, NmF2, which is related to plasma critical frequency, foF2, analyzed in this work. Under this point of view, the spatial and temporal variations in the electron density of the ionosphere are of paramount importance in determining the frequencies available for propagation in point-to-point communications. It was observed that MUF at equatorial region increased over its mean five quietest days reference, during the whole disturbed interval and for several days, while at the southern crest of EIA, the deviation was not so significant. On the other hand, during the main phase of the storm, on 17^{th} March 2015, two remarkable depletions were observed, associated with the F-layer peak height uplifts caused by Prompt Penetration Electric Fields (PPEFs). In this way, the MUF's deviations during PPEF intervals as well as the maximum deviation in each phase of the geomagnetic storm (initial, main, and recovery phase) were evaluated. Additionally, it was noted that the MUF decreases when the height of the F region increases during the disturbed time. In conclusion, the research work showed that geomagnetic storms can severely impact the F-region heights and plasma densities, as well as the MUF available for communications in some periods of the storm. This research can contribute to a better understanding of the influence of geomagnetic storms on radio communication and could be useful to improve prediction models used by Space Weather monitoring and warning centers.

Keywords: Ionosphere. Ionospheric Parameters. Geomagnetic Disturbances. Radio communication. Maximum Usable Frequency (MUF).

ESTUDO DA FREQUÊNCIA MÁXIMA UTILIZÁVEL DURANTE A TEMPESTADE GEOMAGNÉTICA DO DIA DE SÃO PATRICK NO SETOR BRASILEIRO.

RESUMO

Este trabalho apresenta um estudo da variação da Máxima Frequência Utilizável, MUF, durante a primeira tempestade geomagnética intensa do ciclo solar 24, em 17 de março de 2015, conhecida como Tempestade do Dia de Saint Patrick. Para este propósito, foram analisados os seguintes parâmetros ionosféricos: a frequência critica do plasma, foF2, a altura virtual e a altura do pico de densidade da região F, h'F, e hmF2, respectivamente, e a máxima frequência utilizável, MUF, todos fornecidos por Digisondas. Os parâmetros ionosféricos foram registrados por instrumentos instalados em duas regiões representativas no Brasil: na região equatorial, em São Luís, MA (2.5^{o}S, 44.3^{o}W, dip angle 5^{o}S) e na região de baixa latitude nas proximidades da crista sul da Anomalia Equatorial da Ionização, AEI, em Campo Grande, MT (20.44^{o}S, 54.65^{o}W, dip angle 22.3^{o}S). O parâmetro ionosférico MUF é de grande importância para a área de rádio comunicação em alta frequência (HF) e depende fortemente da densidade do plasma ionosférico, NmF2, que está relacionada à frequência crítica de plasma, foF2. Sob este ponto de vista, as variações temporais e espaciais na densidade do plasma ionosférico são de extrema importância na determinação das frequências disponíveis à comunicação ponto a ponto. Observou-se que a MUF na região equatorial se intensificou em comparação com o valor médio dos cinco dias mais calmos, 5QD, durante o período geomagneticamente perturbado, enquanto tal variação não foi tão significante nas proximidades da crista sul da anomalia equatorial da ionização. Por outro lado, durante a fase principal da tempestade geomagnética, no dia 17 de março de 2015, foram observadas reduções significantes no MUF, associadas com a elevação da altura da camada F em dois intervalos, causadas pela ação de campos elétricos de penetração, PPEFs. Deste modo, os desvios percentuais da MUF durante estes intervalos foram determinados, bem como os desvios máximos percentuais em cada fase da tempestade: inicial, principal e de recuperação. Além disso, notou-se que a MUF diminuiu quando a altura da região F aumentou durante o período perturbado pela tempestade. Em conclusão, neste trabalho de pesquisa foi observado que tempestades geomagnéticas podem afetar consideravelmente as alturas e as densidades do plasma ionosférico, alterando as Máximas Frequências Utilizáveis disponíveis para rádio comunicações em determinados períodos. Este trabalho de pesquisa pode contribuir para um melhor entendimento da influência das tempestades geomagnéticas nas rádios comunicações e para melhorar modelos de previsão utilizados por programas de monitoramento e alerta de Clima Espacial.

Palavras-chave: Ionosfera. Parâmetros ionosféricos. Perturbações Geomagnéticas. Comunicação via rádio. Freqüência máxima utilizável (MUF).

LIST OF FIGURES

Page

LIST OF TABLES

Page

LIST OF ABBREVIATIONS

AE – Auroral Electrojet
AL – Auroral Upper
AU – Auroral Lower
CIRs – Corotating Interaction Regions
CMV – Current Mean 5QD Value
CPV – Current Parameter Value
DDEFs – Disturbance Dynamo Electric Fields
EEJ – Equatorial ElectroJet
EFE – Equatorial Fountain Effect
EIA – Equatorial Ionization Anomaly
EMBRACE – Estudo e Monitoramento BRAsileiro do Clima Espacial
EMF – ElectroMotive Force
EUV – Extreme Ultra Violet
HF – High Frequency
HMV – Highest Mean 5QD Value
HPV – Highest Parameter Value
HSS – High Speed Stream
ICMEs – Interplanetary Coronal Mass Ejections
IMF – Interplanetary magnetic field
INPE – Instituto Nacional de Pesquisas Espaciais
IRCC – International Radio Consultative Committee
ITU – International Telecommunication Union
MUF – Maximum Usable Frequency
PPEFs – Prompt Penetration Electric Fields
PRE – PreReversal Enhancement
SFU – Solar Flux Unit
SO – Storm Onset
SPDF – Space Physics Data Facility
SSC – Storm Sudden Commencement
UV – Ultra Violet
WDC – World Data Center

LIST OF SYMBOLS

V_{sw} – Solar wind velocity
$|B|$ – Average magnitude of interplanetary magnetic field
E_y – Interplanetary Electric Field
B_z – Vertical component of the Magnetic Field
R_e – Earth's radius ($R_e = 6371$ km)
B_y – Radial component of the Magnetic Field
B_x – Horizontal component of the Magnetic Field
α – Radiation type
λ – Radiation wavelength
ρ – Charge density
J – Current density
λ – Lyman type of radiation
ε_0 – Permitivity of free space
c – Speed of light
σ – Conductivity
J_H – Hall current
J_P – Pederson current
J_x – Zonal current
σ_p – Pederson conductivity
E_x – Zonal Electric Field
σ_H – Hall conductivity
n – Refractive index
f – Radiowave frequency
ω – Angular frequency
f_p – Plasma frequency
ω_p – Plasma angular frequency($\omega_p = 2\pi f_p$)
ω_H – Electron angular gyrofrequency($\omega_H = 2\pi f_H$)
N_e – Electron density
e – Electronic charge
m_e – Electron mass

CONTENTS

Page

1 INTRODUCTION

In this chapter, few conceptual components that are essential to the development and advancement of this study will be put forward and discussed. The Earth as a planet is known to have a radius of over 6,370 km (3,981 miles), with an atmosphere that is relatively thin stretching upward to a maximum thickness of approximately 500 km (321 miles). This atmosphere is separated into 4 distinct layers (troposphere, stratosphere, mesosphere, and thermosphere) based on its temperature classification, of which the last layer constitutes the larger part of a region known as the Ionosphere. Kirchhoff (1991) affirms that the ionosphere as a region is mainly due to the local electronic density, dominant ions and their production, and loss reactions.

Cander et al. (2003) indicated that one of the primary goals in ionospheric research is to develop the understanding and the means to predict how the ionosphere will respond to changing solar-terrestrial conditions on a day-to-day and an hour-to-hour basis and how these changes will influence radio wave propagation via the ionosphere. In the same vein, Athieno and Jayachandran (2016) stated that the ionosphere plays a significant role as a medium of high frequency (HF) radio propagation that affects communication and remote sensing applications across the world. In this way, the highly variable nature of the ionosphere can be a limitation, and as such, there is so much need to study it.

Russell and Kivelson (1995) suggested some relationship between ionospheric radio wave absorption/propagation and geomagnetic storms. However, in the equatorial region, corresponding ionospheric radio wave absorption studies did not appear to show any explicit relationship between ionospheric radio wave absorption and geomagnetic storm activity. On the other hand, Fejer et al. (1995) showed that ionospheric radio wave absorption in the equatorial region increases after intense storms.

Venkatesh et al. (2017) and Bychkov et al. (2010) described how the Earth's ionosphere was often studied within the context of three latitude zones: high latitudes, middle latitudes, equatorial and low latitudes. It is known that in the equatorial and low-latitude regions, the ionospheric plasma distribution and dynamics are controlled by some electrodynamic processes such as electric fields and plasma drifts. The equatorial and low latitude ionosphere is a region of intense interest, because of the complex dynamical processes and instabilities that occur there (WOHLWEND, 2008).

Based on Bora (2017), the equatorial and low latitude ionospheres have been studied by many ground and space-based experiments as it has many unique features which are not elsewhere. The ionospheric electric field plays a dominant role in low-latitude electrodynamics. The effect of neutral winds, together with diurnal and semi-diurnal tidal components in the atmosphere causes currents in the E region and the production of an electric field.

The consequences of this ionospheric dynamo electric field on the electron density can be investigated using the ionospheric parameters which include F2 layer critical frequency (foF2), minimum virtual height of the F layer trace (h'F), F2 layer peak height (hmF2), and Maximum Usable Frequency (MUF). These parameters of the ionosphere (particularly, of the F region ionosphere) had been studied by many auZhang et al. (2004), Batista et al. (1991), Habarulema et al. (2014), Cherkashin et al. (2003), Pietrella and Perrone (2008), because they determine the morphology, climatology, and variability of the ionosphere (ILYIN et al., 2018). One of those many parameters is the Maximum Usable Frequency (MUF); it is a major characteristic of the radio communication channel or the radio signal path.

MUF is an indicator of space weather in any region of interest, as a result of their importance from a practical point of view for the effective operation of radio communication systems. The values of MUF are determined from ionospheric parameters and mechanisms of radio wave propagation from a transmitter to a receiver (YU et al., 2015; ILYIN et al., 2018). Due to the essential practical nature of the MUF, it is quite paramount to understand its variability and the changes it undergoes during geomagnetically disturbed conditions.

During geomagnetically disturbed periods, the equatorial and low latitude zonal electric fields change drastically due to two major sources, which are Prompt Penetration Electric Field (PPEF) and Disturbance Dynamo Electric Field (DDEF). On the other hand, during geomagnetically quiet periods of time, the low-latitude ionosphere is shielded from high-latitude electric field by the action of region 2 field-aligned currents, but can be influenced by other factors such as, wave activity and others (MENDILLO et al., 2010; ASTAFYEVA et al., 2018).

Under the light of these statements, in this work, the ionospheric response to the first intense geomagnetic storm of solar cycle 24, referred to as Saint Patrick's Day storm, which occurred on March 17th was investigated. For this purpose, some ionospheric parameters, such as foF2 (MHz), MUF (MHz), h'F (km) and hmF2 (km) obtained from ground-based ionospheric sounding, digisonde over two representative regions; a station close to magnetic equator, at São Luis, SL, and a low latitude (around the south crest of EIA), Campo Grande, CG, will be analyzed. The geomagnetic effects on the MUF received a special attention, which of will be of benefit to radio amateurs and space weather forecast programs.

1.1 Geomagnetic disturbances

Ram et al. (2015) explained that geomagnetic disturbances, which are also known as geomagnetic storms, are due to the complex interaction as well as variations between interplanetary magnetic field (IMF) and the geomagnetic field. It has been one of the important Space Weather phenomena that has had the most impact on the thermosphere-ionosphere system, and varies with the latitude, altitude, local time, station and phase of geomagnetic activity, due to the various electrodynamic and neutral interactions that occur.

The variations in the geomagnetic field, such as those due to electromagnetic disturbances during sunspot maximum, may generate currents in Earth's surface, such as electric currents induced in telegraph lines and power-grids, and enhanced corrosion of pipelines (BENESTAD, 2006).

Geomagnetic storms have two main driving sources, Interplanetary Coronal Mass Ejections (ICMEs) and Corotating Interaction Regions (CIRs). The massive streams of solar wind particles transfer the energy and momentum into magnetosphere and subsequent interactions cause intense geomagnetic storms. The ICME-driven geomagnetic storms are generally intense and occur predominantly during the high solar activity periods. On the other hand, the CIR storms are weak in intensity and mainly caused by the High Speed Solar Wind Streams, HSSWSs, from the corotating coronal holes (RAM et al., 2015). Figure 1.1 presents a esquematic representation of the variation of Dst geogmagnetic storms caused by ICMEs (top panel) and CIRs (bottom panel).

During solar minimum, the storm generated by CIRs shows no significant difference for main and recovery phase Jordanova et al. (2020), as shown in Figure 1.1. However, this is not always true, because there are also cases when storms caused by CIRs have recovery phase which can last longer than the main phase.

At the top panel of the Figure 1.1, the storm was driven by ICME with a rapid Sudden Storm Commencement (SSC). The ICME-driven geomagnetic storms are generally intense and occur predominantly during high solar activity periods. Storms generated by ICMEs during solar maximum present larger negative values of Dst and SYM/H index. However, at the bottom panel, the storm was driven by CIR with no SSC.

Figure 1.1 - Geomagnetic storm generated by ICMEs, mainly during solar maximum (top panel) and by CIRs, during solar minimum, the (bottom panel).

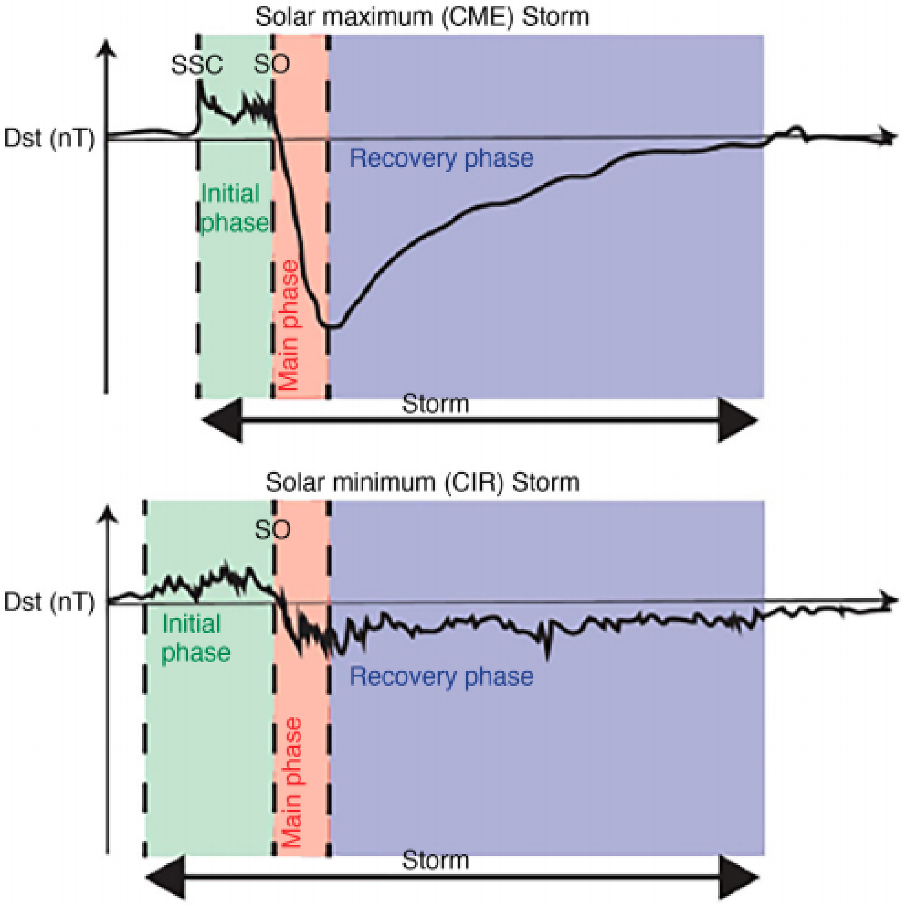

SOURCE: Adapted from Jordanova et al. (2020).

The CIR storms are weak to moderate in intensity and sometimes present a long lasting recovery phase. CIRs are region/surface formed by the interaction between high and low speed streams. They are actually formed formed when high-speed solar wind streams (HSSWs) overtake slow solar wind streams as they propagate outward, as seen in Figure 1.2. From the Figure 1.2, we can see that CIRs produce regions of enhanced density and magnetic field strength in the solar wind near the ecliptic plane. (RAM et al., 2015; SCHWENN, 2006).

Figure 1.2 - An idealized view of a corotating interaction region (CIR) and its evolution from a rectangular speed profile at the Sun into a more gradual speed increase at 1 AU.

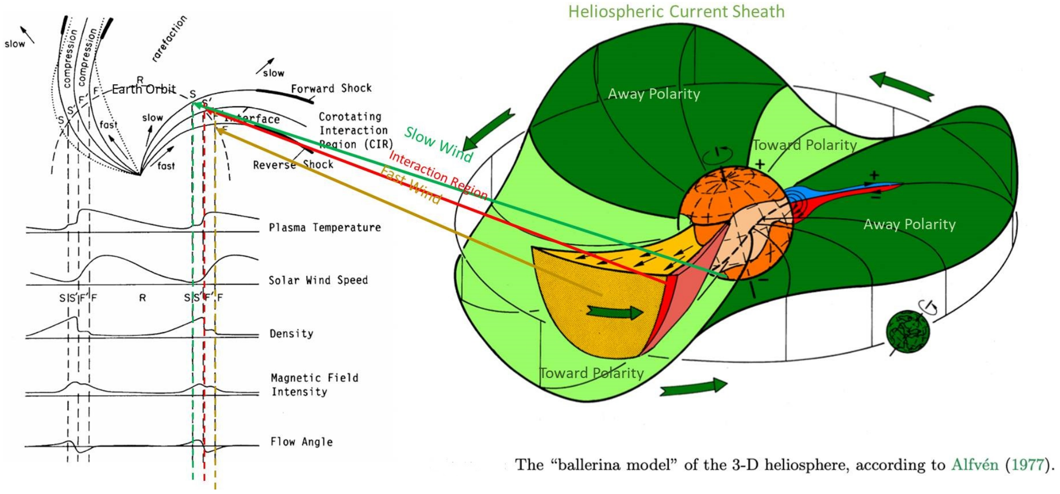

SOURCE: Adapted from Schwenn (2006).

Venkatesh et al. (2017), Ram et al. (2015), Ram et al. (2016) agrees that during geomagnetic storms, the equatorial zonal electric field, which is usually eastward in dayside and westward in nightside experience several changes leading to severe modifications in the equatorial electrodynamic processes. Also, during this geomagnetic storm, the dynamic reconnection between solar wind and Earth's magnetosphere results in the high-latitude electric fields through field aligned currents. The storm time perturbations in the zonal electric field occur mainly due to two important processes. These processes are the two major sources (as mentioned earlier) of equatorial and low latitude zonal electric fields drastic change during disturbed periods:

a) Prompt Penetration Electric Fields (PPEFs), and

b) Disturbance Dynamo Electric Fields (DDEFs).

The electric fields promptly penetrate (PPEFs) into the equatorial latitudes through Earth-ionosphere waveguide (geomagnetic field lines) (VENKATESH et al., 2017; RAM et al., 2015; AKASOFU, 2018; RAM et al., 2016). Bhaskar and Vichare (2013) defined the PPEF as the electric field of solar wind/magnetosphere origin observed equatorward (earthward) of the shielding layer. In the course of the PPEF, two situations can occur, which are known as Undershielding and Overshielding. As reported by

Yeeram (2017), the term undershielding and overshielding are specified when the magnetospheric/solar wind originated electric field is larger and smaller than the shielding layer electric field, respectively.

On the other hand, the energy deposited in the upper atmosphere over high latitudes and the associated Joule and particle heating results in the global variations of the thermospheric wind system, which produces disturbance dynamo electric fields (DDEFs). The DDEFs effects at low latitudes appear few hours after the energy input at high latitudes and often become dominant during the later phase of the storm with non-uniform time delays at different latitudes and lasts for few hours to more than a day.

1.2 Phases of geomagnetic disturbances

Chapman (1935), Akasofu (1977), Akasofu et al. (1963), Akasofu and Chapman (1963), Akasofu (2018) demonstrated that there are three (3) phases of a geomagnetic storm: initial, main and recovery:

- **Initial Phase:** This phase is produced due to compression of the geomagnetic field by a shockwave in the solar wind. It is also referred to as a storm sudden commencement (SSC). It is characterized by two activity indices: Dst increasing by 20 to 50 nT in tens of minutes or its one-minute component SYM/H.

- **Main Phase:** This phase of a geomagnetic storm is defined by Dst decreasing to less than -50nT. The minimum value during a storm will be between -50 and approximately -600nT. The main phase is caused by the ring current around the Earth, and its duration is typically 2-8 hours.

- **Recovery Phase:** This phase is when Dst changes from its minimum value to its quiet time value. It can be a period as short as 8 hours or as long as 7 days.

Figure 1.3 - Phases of geomagnetic storm for the interval period of 16^{th} to 18^{th} March, 2015 using Dst index.

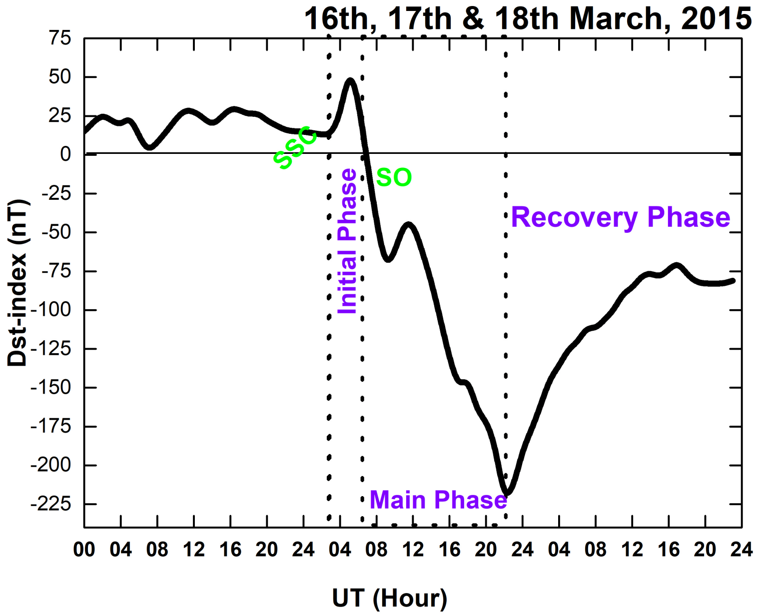

SOURCE: Author.

We can see from Figure 1.3 that SSC started around 03:00 UT (00:00 LT) of 17^{th} indicating the initial phase of the storm till around 07:00 UT (04:00 LT) of 17^{th} when the SO (Storm Onset) started, indicating the main phase.

The minimum SYM/H value during the main phase was approximately -223nT. Recovery phase started at exactly 23:00 UT (20:00 LT) of the same day. The level of geomagnetic disturbance activities is quantified by several indices, each of which emphasizes different aspects of the disturbance. The interplanetary origin of the geomagnetic storm can be identified through the plasma parameters measured, in situ, by satellites that are at the Lagrangian point L1 (point of gravitational equilibrium between Sun and Earth).

The most common parameters used to characterize solar plasma during geomagnetic activity are:

a) Solar wind velocity, V_{sw}, in km/s;

b) Proton density, in n/cc, which indicates when there is compression in the solar charged particles (protons);

c) The magnitude of Interplanetary Magnetic Field, B, measured in nT;

d) Interplanetary Electric Field (E_y), measured in mV/m;

e) The vertical component of the Magnetic Field, B_z; and

f) Finally, the B_x and B_y components of the Interplanetary Magnetic Field.

It is important to know that the E_y together with B_z indicates when there is an electric field prompt penetration.

The geomagnetic indices shown in Figure 1.4 include the following:

- **Kp** (global index);
- **Dst** (low latitudes);
- **Ap** (middle latitudes);
- **AE** (high latitudes); and
- **SYM/H** index.

Menvielle et al. (2011) states that these geomagnetic indices play a significant role in describing the magnetic configuration of the Earth's ionized environment.

Figure 1.4 - Geomagnetic indices variations during March 2015.

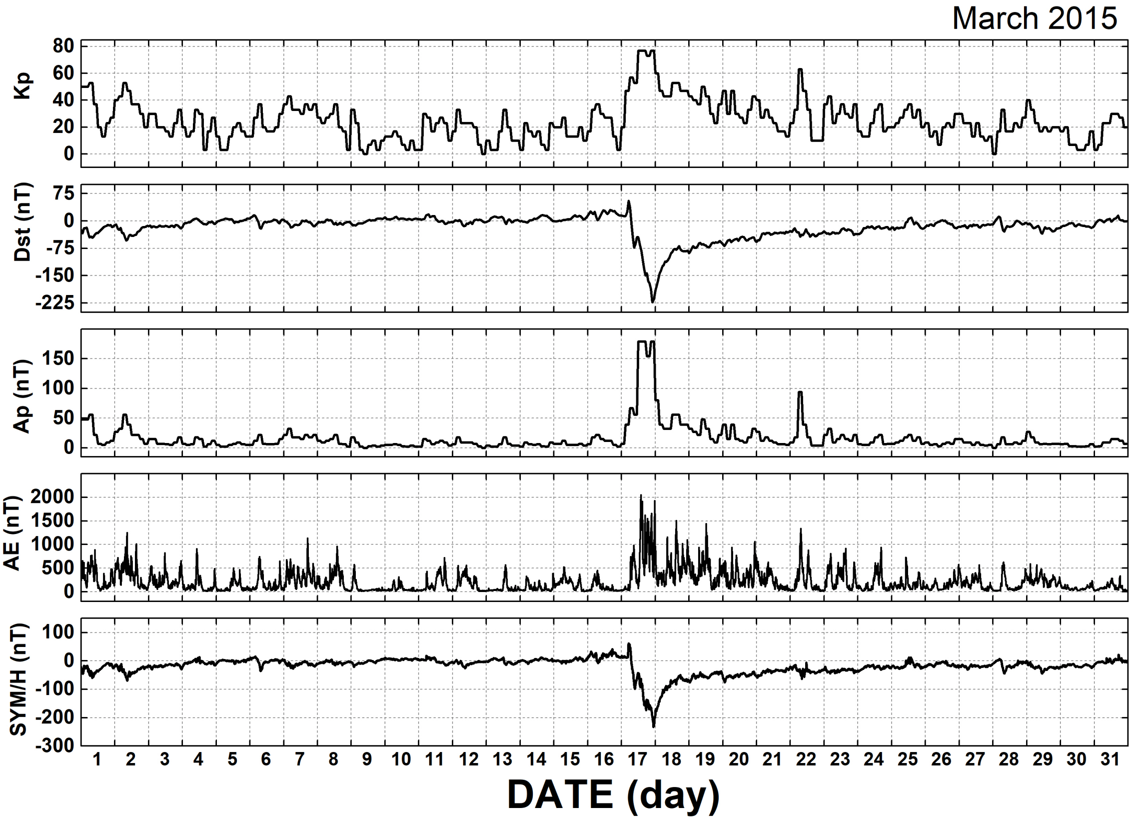

SOURCE: Author.

Kp index: Is obtained from 13 observatories and their data are measured every 3 hours, starting at zero hours. Thus, each day 8 values are provided for Kp. It ranges from 0 to 9 providing a number corresponding to a degree of global disturbance of the geomagnetic field. To be considered disturbed, the Kp index needs to be > 4.

Dst index: The Disturbance Storm Time (Dst) index is used to measure the intensity of the ring current that causes disturbances in the geomagnetic field H. The Dst index is measured from data from 4 observatories located in the earth's equatorial region, and secular and diurnal variations are subtracted from these data. Negative Dst values indicate a magnetic storm is in progress, the more negative Dst is the more intense the magnetic storm.

Ap index: It is obtained from the average of 8 daily values of a-index. The Ap index, which is obtained every 3 hours at stations located at 50° dipolar latitude, provides a daily average level for geomagnetic activity. The Ap index is the linear equivalent of Kp.

AE index: The AE (Auroral Electrojet) index is used to measure geomagnetic activity in the Auroral Zone. Like Dst, it is also obtained through the H component of the magnetic field, but in 12 observatories in the auroral zone in the Northern Hemisphere and can have a resolution of 1 minute or an hour, depending on the agency where the data is captured. It is obtained from the difference of the Indices AU (Auroral Upper) and AL (Auroral Lower).

SYM/H index: The SYM/H index is obtained at medium latitudes and is very similar to Dst, however, with stations at different coordinates and temporal resolution of 1 minute (IYEMORI et al., 2010).

1.3 Motivation

The motivation for this study is based on the huge dependence of the society on communication technology, as almost all our day-to-day activities involve the usage of communication systems, and as a consequence, it is paramount to analyze the basics of MUF (Maximum Usable Frequency). As MUF is the highest radio frequency that can be used for transmission between any two points on the earth's surface via reflection from the ionosphere.

Moreover, the fact that the ionosphere enables radio communications signals to be reflected or refracted back to Earth. Hence, it is crucial to know and analyze what happens to the MUF of the radio signals during some certain state of the ionosphere. The knowledge of the impact of the ionosphere on the radio signals will enable the avoidance of communication lost and plan the best intervals for their transmissions.

1.4 Objectives

The principal objective of this study is to investigate the MUF variation during geomagnetic disturbances in comparison to quiet geomagnetic intervals in two representative regions in Brazil: equatorial region, Sao Luis, and low-latitude region around the crest of EIA, in Campo Grande.

At the same time, the following specific objectives will also be met:

- To recognize the influence of the other ionospheric parameters on the MUF.
- To identify the ionosphere response during geomagnetic activity using ionospheric parameters: foF2, h'F, hmF2, M (D) and MUF.

2 THEORETICAL REVIEW

In this chapter, the theoretical basics of this study's subject matter will be discussed. This chapter provides an overview of the physical and morphological characteristics of the ionosphere, radio wave and its propagation in the terrestrial ionosphere. Section 2.1 provides a brief survey of the Earth's Ionosphere: its formation, structure, and electrodynamics. As the scope of this work entails the equatorial and low latitude ionosphere during geomagnetic disturbed intervals, hence, some characteristics and phenomena of the region are presented. Section 2.2 entails a brief history and some theories of ionospheric radio wave propagation, including the main concepts necessary for the understanding of radio wave and its propagation. Section 2.3 includes the description of HF in the ionosphere. And finally, Section 2.4 describes how the ionosphere concerns the radio communication sector.

2.1 Earth's ionosphere

The Ionosphere is the ionized region of the Earth's upper atmosphere, of which it has the property of reflecting radio waves in the high frequency - HF - band (from 3 - 30 MHz).

The ionosphere is produced by photo-ionization of the ambient atmospheric gases (oxygen and nitrogen) by incoming solar radiation (UV and X-rays). When the solar radiation from the Sun reaches the Earth's atmosphere, the energy is absorbed by the atmospheric components producing heat and ionization, resulting in positive ions and free electrons.

The loss of free electrons occurs by recombination, attachment and diffusion, and so the ionospheric layers tend to be reduced during night times as the loss processes dominate. During the night, without interference from the Sun, cosmic rays ionize the ionosphere, though not nearly as strongly as the Sun.

The 3 steps for the production of heating and ionization during the daylight side of ionosphere which are shown in Figure 2.1 are:

a) Intense incoming radiation is incident on a neutral gas atom or molecules.

b) In the process, part of this radiation is absorbed by the atom or molecule.

c) Then, a free electron and a positively charged ion are produced.

Figure 2.1 - Process of Photoionization and recombination in the Ionosphere. The intense UV radiation from the Sun's atmosphere strikes neutral atoms.

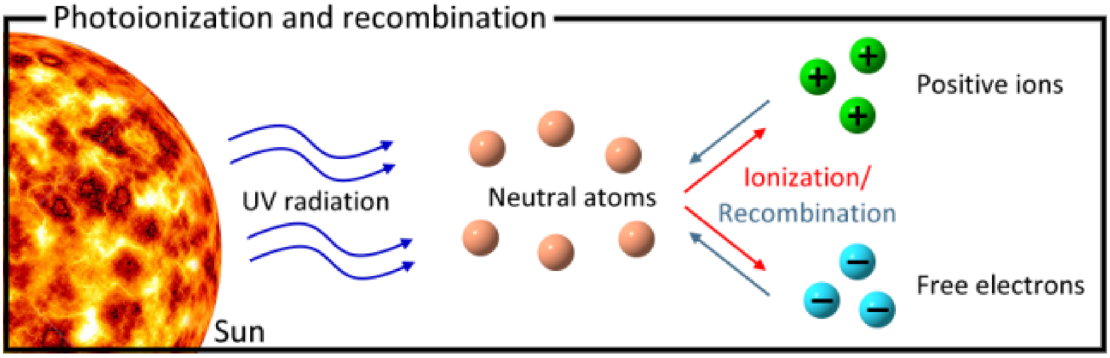

SOURCE: Limberger (2015).

The absorption of some part of this radiation by the neutral atom causes the ionization of the atom into positive ions and free electrons. And then, the free electrons and positive ions can undergo recombination process at the absent of solar radiation (LIMBERGER, 2015). However, it is possible to have recombination processes during the daylight, but in this case the ionization process is more effective than the recombination.

2.1.1 Structure of the Ionosphere

As mentioned earlier, the Ionosphere is a lightly ionized region of the atmosphere lying mainly in the altitude range 60–1500 km (Figure 2.2). The most important mechanism that causes ionization of the ionosphere, at non-auroral latitudes, is the Sun's extreme ultra-violet (EUV), X-ray and Lyman α radiation together with cosmic rays.

Figure 2.2 shows the structure of the ionosphere from 60 Km - 1000 Km approximately, modeled by Kelley (2013), showing that during the nighttime, the ionosphere has three layers, whereas the daytime has four layers.

Figure 2.2 - The structure of the Earth's ionosphere during the daytime and nighttime. The gray lines are during minimum sunspot cycles, while the black lines are during maximum sunspot cycles.

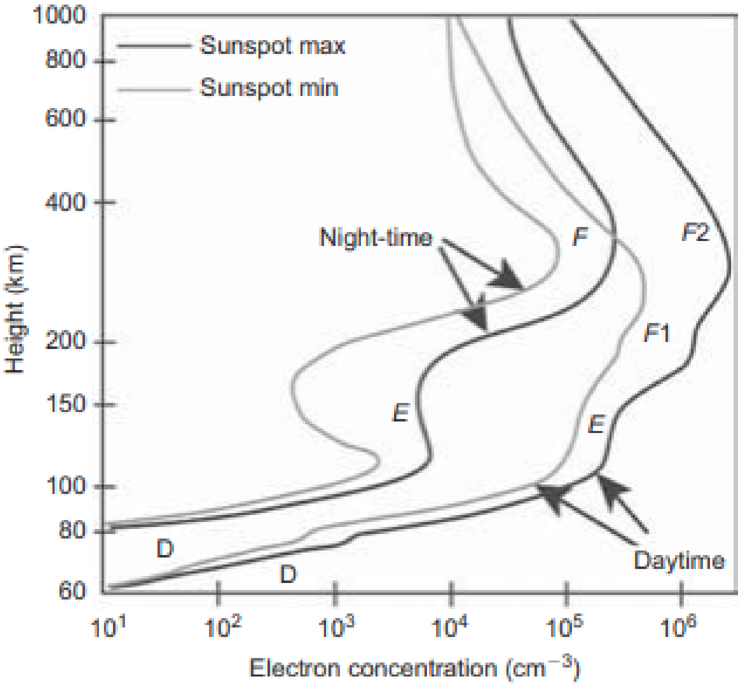

SOURCE: Adapted from Kelley (2013).

The ionospheric layers are identified mainly according to the local electronic density, dominant ions and their production reactions. These regions are named as follows (KIRCHHOFF, 1991; KELLEY, 2009):

- D layer,
- E layer, and
- F layer.

Region D: This region is located between 60 and 90 km in height, approximately. It is formed mainly from the interaction of solar radiation in the X-rays ($\lambda < 10Å$) with the elements: NO, N_2, and O_2.

This region presents a complexity in chemical and photochemical processes which may be characterized by low density and high ionization collisions frequency of electrons with ions and neutral particles.

Region E: This region is located between 90 and 150 km in height, and is formed mainly from the photoionization of neutral constituents by weak X-rays ($\lambda > 10Å$) radiation, solar Lyman-β (1025.7 Å) and Extreme Ultraviolet Radiation ($EUV < 1000Å$) ionizing the O_2, $EUV < 900Å$ ionizing the N_2. The main ions present in the E region are NO^+ and O_2^+.

This region of high conductivity is very important due to the presence of ionospheric electrical currents and the interaction of these currents with the Earth's magnetic field. There is the presence of rare metallic ions such as Fe^+, Mg^+, Na^+, Ca^+ and Si^+. These metallic ions have long life, and they are responsible for the formation of the highly variable dense and thin sporadic E-layers.

Region F: This region is located approximately between 150km and as high as 500km. Its main sources of the ionization are EUV lines and Lyman continuum of hydrogen. The dominant ion is O^+. The F region can be characterized by two other layers, F_1 and F_2. There is also the probability of a third layer (namely F_3) that appears in the equatorial region.

The F_1 layer is defined based on an inflection or a peak in the curve electron density around 180 km. The transition between the processes of linear and quadratic loss occurs in this region. The F_2 layer is located in vicinity of the peak electron density, and it is the region with higher ionization density of the ionosphere. The F_2 may create another layer called F_3. The formation of F_3 is due to the Fountain effect(vertical ExB drift) and the transequatorial wind, which gives rise to the Equatorial Ionization Anomaly (EIA).

2.1.2 Ionospheric electrodynamics

The fundamental mechanisms that control the electrodynamics of the Ionosphere include: neutral wind dynamo theory, ionospheric plasma drifts and conductivities.

Dynamo theory

Astafyeva et al. (2018) explains how the equatorial and low-latitude electric fields are generated primarily by the neutral wind dynamo. This dynamo theory enables the understanding of the generation of electric field, plasma drifts, as well as conductivities that brings about currents.

However, for ionospheric dynamo, the following steps take place:

- The neutral wind blows on the ionized layers, and collision occurs, this collision bring as about motion of ionized gas.
- The motion of ionized gas in the presence of Earth's magnetic field induces

ElectroMotive Force (EMF). The EMF gives rise to electric currents (the dynamo current).

- Due to the variations of horizontal and vertical conductivities, currents cannot flow freely in any direction ($\bigtriangledown \cdot J \neq \bigtriangledown . E = \frac{\rho}{\varepsilon_0}$) So, there is a resultant polarization electric field, which changes the total flow of current.
- The accumulation of these charges produces electric fields. These electric fields are then transmitted across regions through the ionospheric magnetic field lines.

In summary, the main feature of a plasma environment is the zero divergence of current ($\bigtriangledown \cdot J = 0$). However, the current produced in the ionosphere by the neutral wind does not satisfy this condition of current divergence equal to zero. And this failure of the ionosphere to satisfy the plasma environment feature is actually due to the variations in conductivity. Hence, bringing us to the subject "Conductivity".

Conductivity

The conductivity of the ionosphere brings about the ionospheric currents. The ionospheric currents cause a large part of the variation of the geomagnetic field, although most of the geomagnetic field itself is generated by the dynamo action in the Earth's core. According to Maeda (1977), the Ohm's law of the ionospheric dynamo is given by the following equation:

$$j = (\sigma) \left[\overrightarrow{E} + \overrightarrow{V_n} \times \overrightarrow{B} \right] \tag{2.1}$$

where,

j is the density of current flowing in the dynamo layer, (σ) is the conductivity tensor, $\overrightarrow{E}$ is the electrostatic field generated by the polarization due to the differential motions of ions and electrons, $\overrightarrow{V_n}$ is the velocity of neutrals, and $\overrightarrow{B}$ is the geomagnetic flux density.

The currents flow according to Ohm's law, but the electric conductivity is anisotropic because of the effect of the geomagnetic field. Tiwari (2015), the ionospheric conductivity tensor with its x-axis along B_0 is given as:

$$\sigma = \begin{bmatrix} \sigma_P & -\sigma_H & 0 \\ \sigma_H & \sigma_P & 0 \\ 0 & 0 & \sigma_0 \end{bmatrix}. \tag{2.2}$$

The three conductivities are: Parallel, Pedersen and Hall conductivities. The International System of unit for conductivity is Siemens per meter (S/m) or mho.

- Parallel conductivity is the conductivity that is in the direction parallel to the magnetic field line and denoted as "σ_0". This is the same as that when there is no magnetic field, and much larger than Pedersen and Hall conductivities in the ionosphere.

- Pedersen conductivity is the conductivity that is in the direction perpendicular to the magnetic field and parallel to the electric field. It is denoted as "σ_P".

- Hall conductivity is the conductivity that is in the direction perpendicular to both the magnetic and electric fields. It is denoted as "σ_H". In the ionosphere, this conductivity is due to the drift motion of the electron (ExB drift) and maximum in the E region where only electron practically drifts to the direction of ExB.

Ionospheric Plasma Drifts

The ionospheric plasma drifts; in particular the vertical drift due to $E \times B$ force allows a better understanding of the spatial and temporal distribution of the ionospheric plasma. Along the magnetic field line (magnetic flux tube), the equatorial zonal and vertical drifts are given by the vertical and zonal electric fields, respectively (SOUZA, 2019).

The quiet time vertical and zonal components of the dynamo electric fields cause the ionospheric plasma to drift westward and upward, respectively, during the daytime and eastward and downward at nighttime. During magnetic disturbances, these drifts can be drastically modified by disturbance zonal electric fields of magnetospheric origin and of disturbance ionospheric dynamos (ABDU et al., 1990).

The studies by Carrasco et al. (2005) have revealed that the storm time disturbance zonal electric field that drives disturbance vertical drift can modify also the vertical electric field that drives zonal plasma drift with significant impacts on other equatorial phenomena such as the plasma flow dynamics, and sporadic E layer (Es) development.

Abdu et al. (1981) showed that while a westward electric field can cause a downward plasma drift, an eastward disturbance electric field can produce an upward vertical drift of the ionospheric plasma.

Near the magnetic equator, ionospheric drifts occur in both E and F regions, which is a mainly westward by day and eastward by night.

Figure 2.3 presents the temporal variation of vertical and zonal drifts. The zonal drift decreases towards the local noon, whereas the vertical drift experiences an increase during this time period. Around 18:00LT, it can be seen that the vertical drift (ExB) experiences an evening prereversal enhancement.

Figure 2.3 - The temporal variation of vertical and zonal drifts. The zonal drift decreases towards the local noon, whereas the vertical drift experiences an increase during this time period. Around 18:00LT, it can be seen that the vertical drift (ExB) experiences an evening prereversal enhancement.

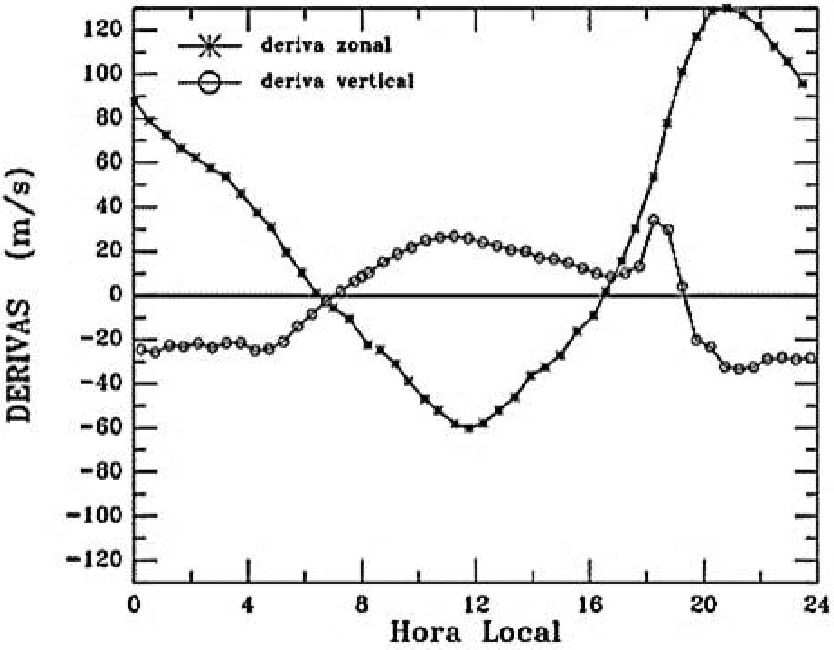

SOURCE: Adapted from Souza (2019).

2.1.3 Ionospheric phenomena associated with ExB vertical drift

The ionosphere of the equatorial and low latitude regions present some peculiar characteristics and phenomena due the horizontal configuration of the geomagnetic field, these phenomena include: the plasma Fountain effect, the Equatorial Ionization Anomaly (EIA), plasma structuring leading to the development of plasma irregularities, or Equatorial Plasma Bubbles (SOUZA, 2019), and equatorial electrojet current system.

The horizontal orientation of the geomagnetic field at the magnetic equator is the basic reason for the upward vertical plasma drift in the equatorial and low-latitude ionosphere. This upward vertical plasma drift is the main factor responsible for prereversal enhancement (PRE) and plasma irregularity generation (FEJER et al., 1999; BALAN; BAILEY, 1995).

Hence, in other words, it can be said that the active nature of the equatorial and low-latitude ionosphere is characterized by the Equatorial ElectroJet (EEJ), Equatorial Fountain Effect (EFE) and Equatorial Ionization Anomaly (EIA).

Pre Reversal Enhancement (PRE)

According to Kelley (2009), near the solar terminator by the sunlit side, the F region dynamo generates the field E_z around 18:00 that is not so small. This field is mapped to the E region and pointing towards the equator (E_y) as shown in Figure 2.4.

The field E_y in the presence of the geomagnetic field gives rise to a Hall current (J_H) westward. But, as the night side the conductivity is low, there is an accumulation of negative charges creating a field E_p in the terminator and, consequently, a current J_P to cancel J_H.

The field E_p is mapped back to producing the F region vertical drift increases and then decreases rapidly after due to the field inversion which occurs when night comes. This vertical drift maximum before its inversion around 18:00 hours, it is known as Pre-Reversal Enhancement.

Figure 2.4 shows that the downward electric field (E_z) causes large eastward electric fields (intensified). So, the intensified eastward electric field enhances vertical plasma drift around local sunset.

Figure 2.4 - Simplified model of the F-region prereversal enhancement driven by a uniform F-region wind, U.

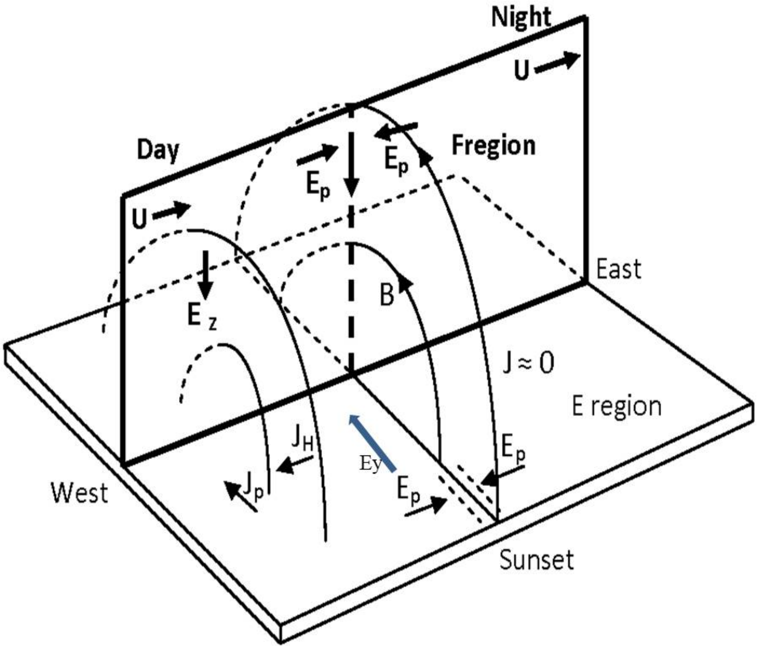

SOURCE: Adapted from Kelley (2009).

Equatorial Fountain Effect & Equatorial Ionization Anomaly (EFE & EIA)

In conjunction with the horizontal northward geomagnetic field at equatorial latitudes, the ionospheric plasma is lifted upward by vertical E×B drift (RUSSELL; KIVELSON, 1995). Once the plasma is transported to higher altitudes, as seen in Figure 2.5, it diffuses downward along the geomagnetic field lines into both hemispheres due to gravitational and pressure gradient forces.

Figure 2.5 shows that this combination of electromagnetic drift and diffusion produces a fountain like pattern of plasma motion called the Equatorial Fountain Effect, EFE, leaving region around the magnetic equator with lower electron density concentration and higher electron density concentrations at the crests or equatorial anomaly regions.

Figure 2.5 - The formation of Equatorial Ionization Anomaly is driven mainly from the removal of plasma from around the equator by the upward E×B drift creating the trough and consequently the crests with small accumulation of plasma within ±20° magnetic latitudes, as depicted by (MATHIS, 2013).

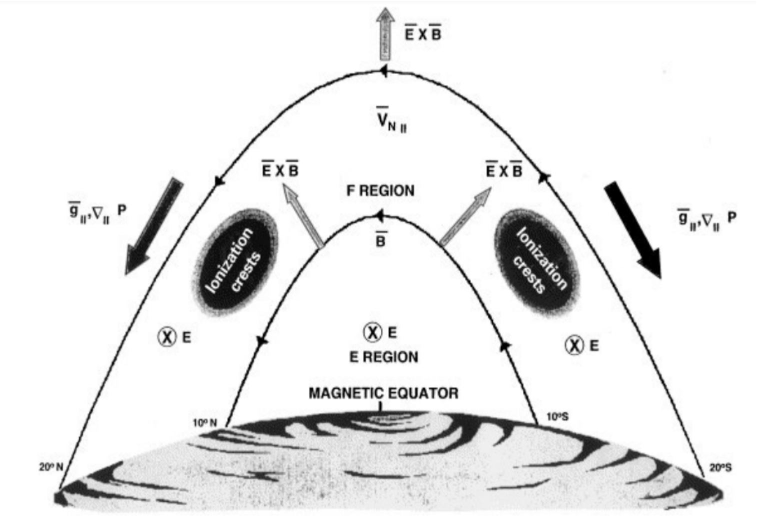

SOURCE: Adapted from Mathis (2013).

This implies that ionospheric effects on radio communication for example, are higher around the equatorial crests than at the trough region or magnetic equator. In short, the EIA is formed as a result of the diurnal variation of the zonal electric field, which primarily points eastward during the day and reverses westward at night.

Equatorial ElectroJet (EEJ)

The E region dynamo refers to the phenomenon in which electric current flows through the E region during the daytime, resulting in polarization electric field, as seen in Figure 2.6.

Therefore, due to the cowling conductivity $\left[1 + \frac{\sigma_H^2}{\sigma_P^2}\right]$, zonal current

$J_x = \sigma_p E_x \left[1 + \frac{\sigma_H^2}{\sigma_P^2}\right]$ is intensified. Over the geomagnetic equator, in the E region dynamo, the zonal electric field is perpendicular to the geomagnetic field; as such the zonal current reaches its maximum enhancement.

Figure 2.6 shows that the zonal current that is intensified in the E region during daytime is known as Equatorial ElectroJet (EEJ). This current flows eastward during the day and westward at night.

Figure 2.6 - Mechanism of the equatorial electrojet current flow in the E-region is described in three steps.

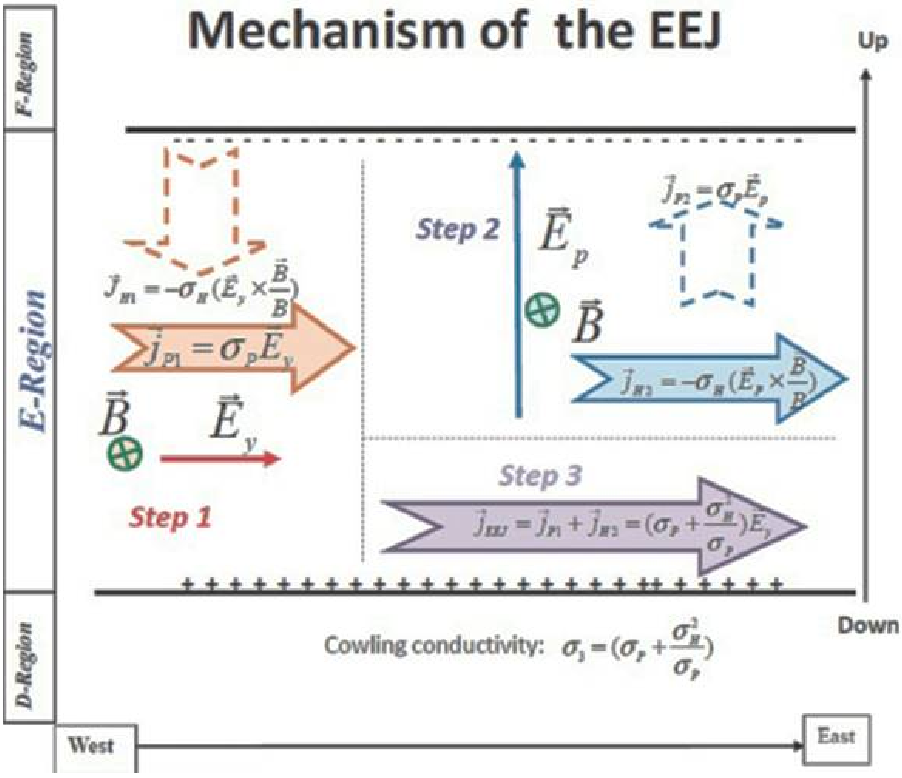

SOURCE: Adapted from Grodji et al. (2017).

2.2 Ionospheric radio wave propagation

In 1901, Marconi demonstrated that radio waves could be propagated to great distances over the earth's surface. He succeeded in transmitting radio signals across the Atlantic, and this surprising result, of propagation to such distances around the curvature of the earth posed a major problem to the theoretical physicists of that time. Radio waves are defined in the International Telecommunication Union (ITU) Radio Regulations as "electromagnetic waves of frequencies arbitrarily lower than 3,000 GHz, propagated in space without artificial guide". This covers the frequency range where the characteristics of propagation in the ionosphere permit communication to a useful distance.

Kennelly (1902), Heaviside (1902) independently suggested that the existence of a conducting ionized layer in the upper atmosphere would explain the observations of Marconi. When investigating the behavior of radio waves in an ionized medium, found the refractive index to be less than unity, thus allowing the possibility of reflection. However, most scientists favored the explanation of Marconi's observations based on the diffraction of the waves around the conducting surface of the earth (ECCLES, 1912; KENNELLY, 1902).

From the beginning, it has been the practical use of the propagation of electromagnetic waves over long distances, together with the ability to modulate the waves and thus transfer information, which has provided the incentive for the development of radio and electronic technologies. This, in turn, has driven a need to extend knowledge of the propagation environment, and to characterize the transfer function of the radio channel, seeking to provide greater communication bandwidths and greater quality of service. The profile of electron density in the ionosphere acts as a reflecting layer capable of reflecting signals at High Frequency (HF) and lower frequencies to Earth (ECCLES, 1912).

The next section will focus on the propagation of HF (2-30 MHz) signals in the ionosphere.

2.3 HF in the ionosphere

On 31 December 1901, Marconi succeeded in transmitting a radio signal from Cornwall, England, to Newfoundland, Canada, proving that radio waves could travel around the curvature of the Earth. Independently, Kennelly (1902), Heaviside (1902) suggested that signals were reflecting from a conducting layer of atmospheric ions at an altitude of approximately 80 km.

Ionospheric propagation is the main mode of radio wave propagation used in the HF portions of the radio spectrum. HF propagation using the ionosphere is widely used as a form of radio communications, due to some advantages, which include that it is not expensive, and can provide a useful back-up in case satellite communications fail. However, one disadvantage is that it is not as reliable as satellite communications (CHUKWUMA, 2018).

Haigh and Cargill (2015) affirm that the study of high frequency radio wave propagation has been based on the ray theory evaluation of the propagation characteristics of the wave. Communications and data transmission systems, using High-Frequency radio waves, require an assessment of the propagation parameters, in particular, the signal strength. And this HF communications and radar systems are, of course, dependent on the ionosphere for long-distance operation, which is the actual reason that monitoring the ionosphere is of concern.

In the following sub-section, the propagation of HF radio waves and their reflection by the ionosphere will be briefly discussed.

Reflection of HF radio waves

The passage of HF radio wave through the ionosphere is influenced by many factors, but predominantly the electron density profile. Zawdie et al. (2017) asserts that the ionospheric propagation of HF radiowaves is very much dependent on the electron density in the ionosphere and the collision frequency between electrons and neutrals. Due to the ability of ionized atmospheric gases to refract HF radio waves, the ionosphere can reflect radio waves directed into the sky back toward the Earth. Radio waves directed at an angle into the sky can return to Earth beyond the horizon. The amount of radio waves reflection that occurs depends on three main factors:

- The density of ionization of the layer (electron density profile),
- The angle at which the wave enters the layer, and
- The refractive indices of the radio wave.

The refractive index of an electromagnetic wave propagating through an isotropic ionized medium in the presence of a magnetic field is given by the Appleton-Hartree formula (ZAWDIE et al., 2017):

$$n^2 = 1 - \frac{X}{1 - iZ - \frac{Y_T^2}{2(1-X-iZ)} \pm \left[\frac{Y_T^4}{4(1-X-iZ)^2} + Y_L^2\right]^{1/2}} \tag{2.3}$$

where:

n is the complex refractive index of the propagating radio wave;

$$i = \sqrt{-1} \tag{2.4}$$

$$X = \frac{\omega_p^2}{\omega^2} = \frac{N_e e^2}{\varepsilon_0 m_e \omega^2} \tag{2.5}$$

$$Y = \frac{\omega_H}{\omega} = \frac{eB}{m_e \omega} \tag{2.6}$$

$$Z = \frac{\nu}{\omega} \tag{2.7}$$

ν is the electron collision frequency; this is the collision frequency between electrons and neutrals which is dependent on the atmospheric density,

f and ω are the radiowave frequency and angular frequency respectively ($\omega = 2\pi f$),

f_p and ω_p are the plasma frequency and plasma angular frequency respectively ($\omega_p = 2\pi f_p$),

ω_H is the electron angular gyrofrequency,

N_e is the electron density,

e is the electronic charge,

m_e is the electron mass,

ε_0 is the permittivity of free space, and

B is the magnetic field.

The subscripts L and T in Equation (2.3) refer to longitudinal and transverse components relative to the direction of phase propagation. The ± sign in the Appleton-Hartree of Equation (2.3) indicates that two polarizations of the radio wave can exist, termed the ordinary and extraordinary waves.

Two simplifying cases can be considered to illustrate the basic principles of propagation in the ionosphere:

- When there is negligible magnetic field, then we have that $Y_T = Y_L = 0$, and
- When there is negligible collision frequency, then we have that $Z = 0$.

In the simple case of anisotropic ionosphere, with negligible magnetic field and no collisions, the complex refractive index of Appleton-Hartree (Equation 2.3) reduces to the real expression:

$$n^2 = 1 - X = 1 - \frac{f_p^2}{f^2} \tag{2.8}$$

For vertically propagating waves, reflection occurs when $n = 0$, which implies that we get:

- For positive sign, $X = 1$, the plasma frequency and the radio wave frequency are equal, $f = f_p$. This wave is called the ordinary wave.
- For negative sign, we get extraordinary wave with two conditions. When wave frequency is greater than gyrofrequency ($f > f_p$), we have that $X = 1 - Y$, and when wave frequency is below gyrofrequency ($f < f_p$), then we get that $X = 1 + Y$.

2.4 Ionospheric radio propagation & communication

The ionospheric propagation of radio waves is affected by free electron concentration, the geomagnetic field, and the collisions between charged and uncharged particles. The Earth's magnetic field causes the incident wave to be doubly refracted within the ionosphere. While, the presence of the free electrons in the ionosphere is what effects radio signals across several bands of the spectrum from 3 kHz to 30GHz. The alternating electric field of the radio wave causes the motion in the free electrons (FAGRE et al., 2019).

There are several paths that a radio wave can take between transmitter and receiver, with different reflection heights, and possibly with intervening reflections from the ground. These paths are denoted modes and are labelled by the number of hops and the region of the ionosphere from which reflection occurs (PIETRELLA; PERRONE, 2008).

A transmitted HF signal can be reflected from more than one of the several layers in the ionosphere. The transmission of a single pulse of energy, as shown in Figure 2.7 is consequently received as a number of pulses which may be distinct or which may overlap.

Figure 2.7 shows that using HF ionospheric propagation, the radio signals leave the transmitting radio antenna on Earth's surface and travel towards the ionosphere where some of these are returned to Earth.

Figure 2.7 - HF radio wave signal path in the ionosphere. The ionosphere acts as a vast reflective surface that encompasses the Earth's atmosphere.

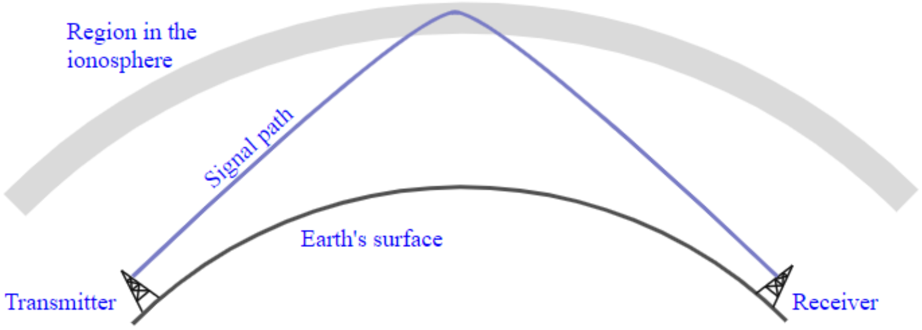

SOURCE: Adapted from Barclay (2003).

The ionosphere plays a great role in different sectors that use the radio communication system, through reflecting the radio signals back to the receivers. However, its effectiveness depends on the frequency of the transmitted signal.

When the radio waves are transmitted from the surface of the Earth, they are reflected back from the ionosphere and able to reach the transmitter. So the ionosphere has practical importance because, among other functions, it influences radio propagation to distant places on the Earth. The passage of a radio wave through the ionosphere is influenced by many factors, but predominantly the electron density profile. The electron density is related to the refractive index and some ionospheric parameters (BARCLAY, 2003).

3 DATA AND METHODOLOGY

3.1 Period of study

In order to understand the influence of geomagnetic storm on the equatorial ionosphere, especially in the Maximum Usable Frequency, MUF, the solar maximum year of 2015 was chosen, because it was the second pick of the sunspot solar activity. The month of study was taken to be March, in view of the fact that, it is the month with the first intense geomagnetic storm of solar cycle 24.

For the month mentioned above, storm interval of 9 geomagnetically disturbed days plus one day before the storm, and 5 geomagnetically quietest days were selected. According to Lang (2001), the currents associated with solar wind and magnetosphere interactions are highly variable; the period of weak interactions or no interactions at all are called geomagnetically quiet days, and the period of strong interactions are called geomagnetically disturbed days. In order to investigate the effects of the storm on the ionosphere, geomagnetically quiestest days were taken for comparison.

The storm interval days were taken using the hourly equatorial provisional Dst index provided by World Data Center (WDC) for geomagnetism, Kyoto (`http://wdc.kugi.kyoto-u.ac.jp/`) as seen in Figure 3.1.

The storm commenced on the 17^{th}, however, 16^{th} was chosen as the first day, down to 25^{th} as the last day in the month of March 2015, as can be seen by the blue rectangle in the Figure 3.1. We can see that a day before the storm commences and few days of recovery phase were all considered to be analyzed.

Figure 3.1 - The Dst (provisional) index for March 2015. The red rectangles show the 5 quietest days (5QD), and the blue rectangles show the storm interval.

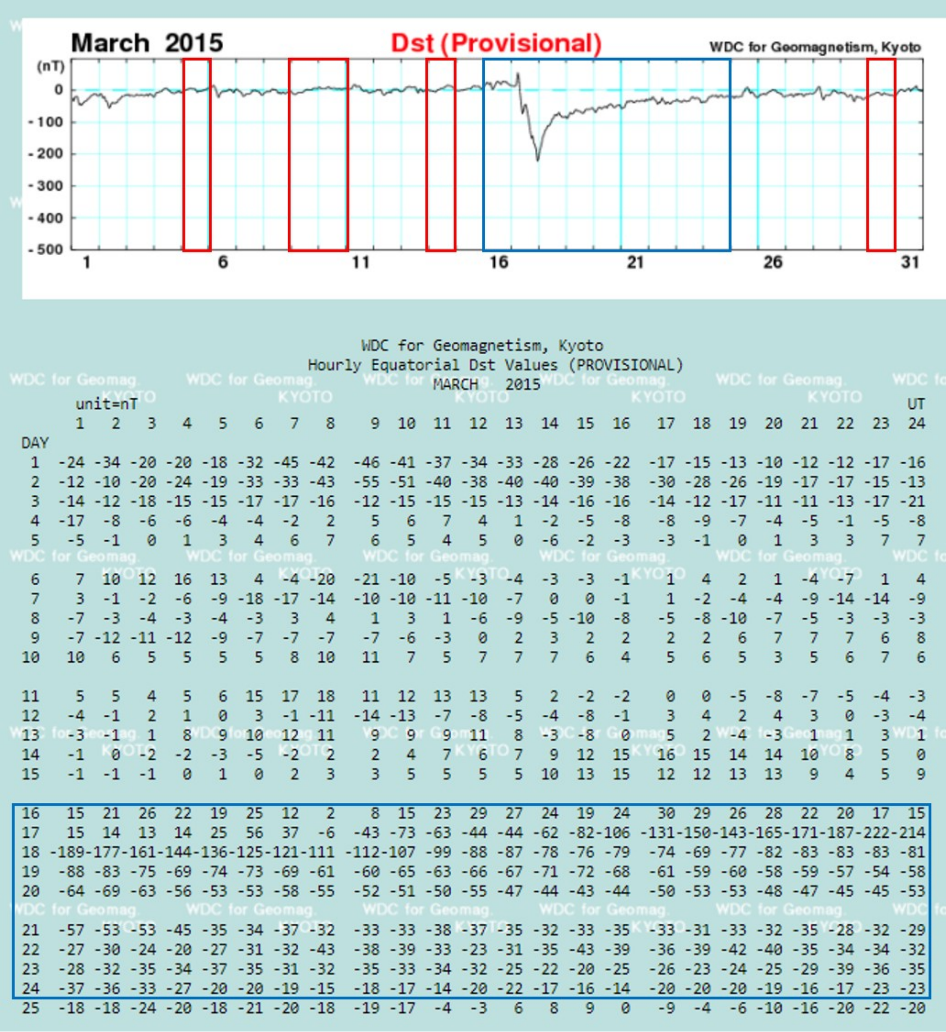

WDC for Geomagnetism, Kyoto
Hourly Equatorial Dst Values (PROVISIONAL)
MARCH 2015
unit=nT

DAY	1	2	3	4	5	6	7	8	9	10	11	12	13	14	15	16	17	18	19	20	21	22	23	UT 24
1	-24	-34	-20	-20	-18	-32	-45	-42	-46	-41	-37	-34	-33	-28	-26	-22	-17	-15	-13	-10	-12	-12	-17	-16
2	-12	-10	-20	-24	-19	-33	-33	-43	-55	-51	-40	-38	-40	-40	-39	-38	-30	-28	-26	-19	-17	-17	-15	-13
3	-14	-12	-18	-15	-15	-17	-17	-16	-12	-15	-15	-15	-13	-14	-16	-16	-14	-12	-17	-11	-11	-13	-17	-21
4	-17	-8	-6	-6	-4	-4	-2	2	5	6	7	4	1	-2	-5	-8	-8	-9	-7	-4	-5	-1	-5	-8
5	-5	-1	0	1	3	4	6	7	6	5	4	5	0	-6	-2	-3	-3	-1	0	1	3	3	7	7
6	7	10	12	16	13	4	-4	-20	-21	-10	-5	-3	-4	-3	-3	-1	1	4	2	1	-4	-7	1	4
7	3	-1	-2	-6	-9	-18	-17	-14	-10	-10	-11	-10	-7	0	0	-1	1	-2	-4	-4	-9	-14	-14	-9
8	-7	-3	-4	-3	-4	-3	3	4	1	3	1	-6	-9	-5	-10	-8	-5	-8	-10	-7	-5	-3	-3	-3
9	-7	-12	-11	-12	-9	-7	-7	-7	-7	-6	-3	0	2	3	2	2	2	2	6	7	7	7	6	8
10	10	6	5	5	5	5	8	10	11	7	5	7	7	7	6	4	5	6	5	3	5	6	7	6
11	5	5	4	5	6	15	17	18	11	12	13	13	5	2	-2	-2	0	0	-5	-8	-7	-5	-4	-3
12	-4	-1	2	1	0	3	-1	-11	-14	-13	-7	-8	-5	-4	-8	-1	3	4	2	4	3	0	-3	-4
13	-3	-1	1	8	9	10	12	11	9	9	9	11	8	-3	-8	0	5	2	-4	-3	1	1	3	1
14	-1	0	-2	-2	-3	-5	-2	2	2	4	7	6	7	9	12	15	16	15	14	14	10	8	5	0
15	-1	-1	-1	0	1	0	2	3	3	5	5	5	5	10	13	15	12	12	13	13	9	4	5	9
16	15	21	26	22	19	25	12	2	8	15	23	29	27	24	19	24	30	29	26	28	22	20	17	15
17	15	14	13	14	25	56	37	-6	-43	-73	-63	-44	-44	-62	-82	-106	-131	-150	-143	-165	-171	-187	-222	-214
18	-189	-177	-161	-144	-136	-125	-121	-111	-112	-107	-99	-88	-87	-78	-76	-79	-74	-69	-77	-82	-83	-83	-83	-81
19	-88	-83	-75	-69	-74	-73	-69	-61	-60	-65	-63	-66	-67	-71	-72	-68	-61	-59	-60	-58	-59	-57	-54	-58
20	-64	-69	-63	-56	-53	-53	-58	-55	-52	-51	-50	-55	-47	-44	-43	-44	-50	-53	-53	-48	-47	-45	-45	-53
21	-57	-53	-53	-45	-35	-34	-37	-32	-33	-33	-38	-37	-35	-32	-33	-35	-33	-31	-33	-32	-35	-28	-32	-29
22	-27	-30	-24	-20	-27	-31	-32	-43	-38	-39	-33	-23	-31	-35	-43	-39	-36	-39	-42	-40	-35	-34	-34	-32
23	-28	-32	-35	-34	-37	-35	-31	-32	-35	-33	-34	-32	-25	-22	-20	-25	-26	-23	-24	-25	-29	-39	-36	-35
24	-37	-36	-33	-27	-20	-20	-19	-15	-18	-17	-14	-20	-22	-17	-16	-14	-20	-20	-20	-19	-16	-17	-23	-23
25	-18	-18	-24	-20	-18	-21	-20	-18	-19	-17	-4	-3	6	8	9	0	-9	-4	-6	-10	-16	-20	-22	-20

SOURCE: Adapted from the WDC website (2021).

The Table 3.1 and the 5 small rectangles in Figure 3.1 shows the 5 quietest days (their average mean was taken) which were chosen using the geomagnetic index Kp as a reference according to IAGA classification `http://wdc.kugi.kyoto-u.ac.jp/qddays/index.html`.

Table 3.1 - The 5 quiestest day (5QD) for the month of study.

Months	Q1	Q2	Q3	Q4	Q5
March	10	30	5	14	9

3.2 Equatorial and low-latitude region of study

The two areas of study are: an equatorial station in São Luís and a low-latitude site, around the south crest of EIA, in Campo Grande.

São Luís station is located in geographical coordinates 2.5^{o}S and 44.3^{o}W, while the magnetic inclination (dip angle in 2015) was approximately 5^{o}S, which implies that it can be considered as an equatorial region station. On the other hand, Campo Grande station is located in geographical coordinates 20.44^{o}S and 54.65^{o}W, while the magnetic inclination (dip angle in 2015) was approximately 22.3^{o}S, which implies that, it can be considered as a low-latitude station.

Figure 3.2 - The geographic coordinate locations of the two areas of study, showing Sao Luis and Campo Grande as the equatorial and low-latitude stations, respectively.

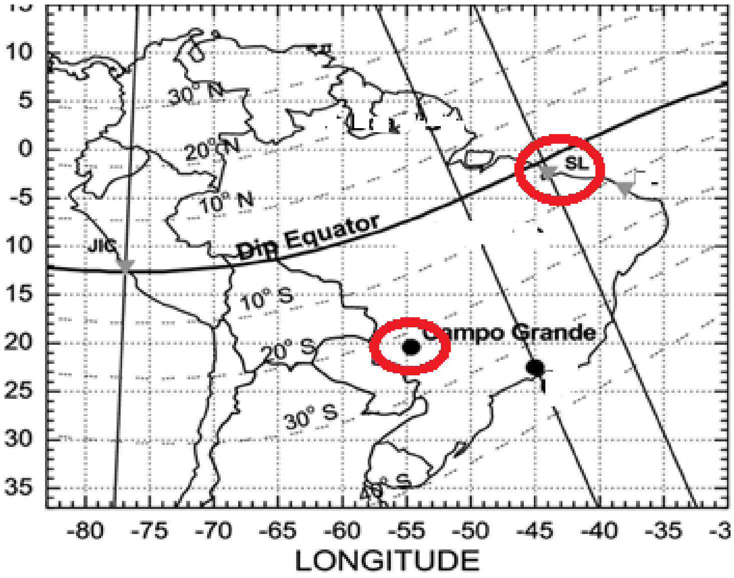

SOURCE: Abdu et al. (1990).

3.3 Data acquisition

For the purpose of this work, the data used were ground-based and space-based. The ground-based data was for the ionospheric parameters, while the space-based data was for the solar and geomagnetic index parameters.

For the ionospheric parameters, the Digisonde data were provided by Space Weather Data Share, and were downloaded from Estudo e Monitoramento BRAsileiro do Clima Espacial (EMBRACE), Instituto Nacional de Pesquisas Espaciais (INPE) website `http://www2.inpe.br/climaespacial/SpaceWeatherDataShare/search/`.

For the solar and geomagnetic index data, the OMNIWeb Plus data provided by the Space Physics Data Facility (SPDF) of NASA's Goddard Space Flight Center were downloaded from `http://omniweb.gsfc.nasa.gov` .

3.4 Instrumentation

In this section, the instruments used for this study are presented and data collected are described. The ionospheric parameters used for this study were obtained by the instrument known as Ionosonde.

The most continuous ionospheric sounding is provided by Ionosondes. Ionosonde is a high frequency radar sounding remote instrument used for monitoring and ionosphere research, which measures the electronic density profile as a function of frequency (SANTOS, 2013). This ground based ionospheric sounder gets the information about the ionosphere up to the F2 layer peak density. The Ionosonde is a high frequency radar composed of a set of antennas and a transmitter-receiver system. The transmitter emits electromagnetic waves (pulses of energy) to the ionosphere in the radio frequency range (between 1 to 30MHz) and the receiver records the intensity of the pulse reflected in the layers ionosphere. In this frequency range, the signal undergoes successive refractions until reflected by the ionospheric medium (charged species). The return signal (echo) or backscattered signal, carries very useful information about the ionosphere, the most important being the numerical density of electrons (n_e). The time between the transmission of the pulse and its return to the receiver is recorded by the Ionosonde providing the height at which the pulse reflection occurred (RUSSELL; KIVELSON, 1995).

With technological advances, ionospheric sounding techniques have evolved, and the analog Ionosonde have been replaced by digital Ionosonde (Digitally Integrating Goniometric IonoSONDE or DIGISONDE), where all the control over the processing and data storage has gone digital. With this new instrument (Digisonde), it is possible to expand the number of ionospheric data to be observed and the cost maintenance has also been reduced.

One of the most popular models is DPS4 (ODRIOZOLA, 2013), and it is installed at the two ionospheric stations that generated the data used in this research study. One of the most useful characteristics of the DPS4 Digisondes is that they allow the identification for the direction of return for the echoes emitted by the ionosphere.

Figure 3.3 - DPS4 Digisonde that is currently installed in the ionospheric station of São Luís.

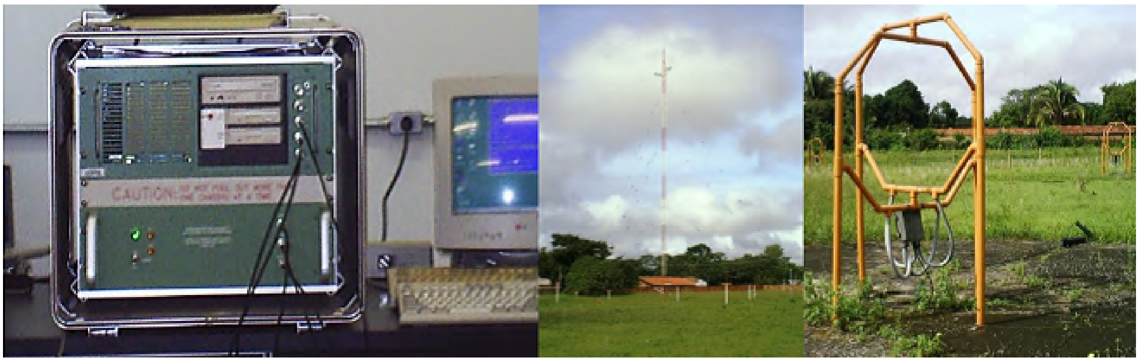

SOURCE: Santos (2013).

The Digisondes in São Luís and Campo Grande perform an ionosphere survey regularly every 10 minutes. The Digisonde has a radius horizontal covering of the ionosphere approximately 1260 km in São Luís, although this depends on the emission pattern of the antenna used. At both stations, the survey altitude resolution is 5 km (ODRIOZOLA, 2013).

3.4.1 Extraction of the ionospheric parameters

The work done with the Digisonde data uses Sao Explorer software. This software is installed on the computer as part of the Digisondes DPS4 equipment, but can also be downloaded from the internet (SAO EXPLORER, 2016).

The Sao Explorer program loads the raw data generated by Digisonde, the parameters to be processed are then chosen, as shown at the list of parameters in the opening window of Sao Explorer, according to the Figure 3.4 (parameters and colors can be selected by the user).

Figure 3.4 - Interface of Sao Explorer software showing the ionospheric characteristic sets that can be selected.

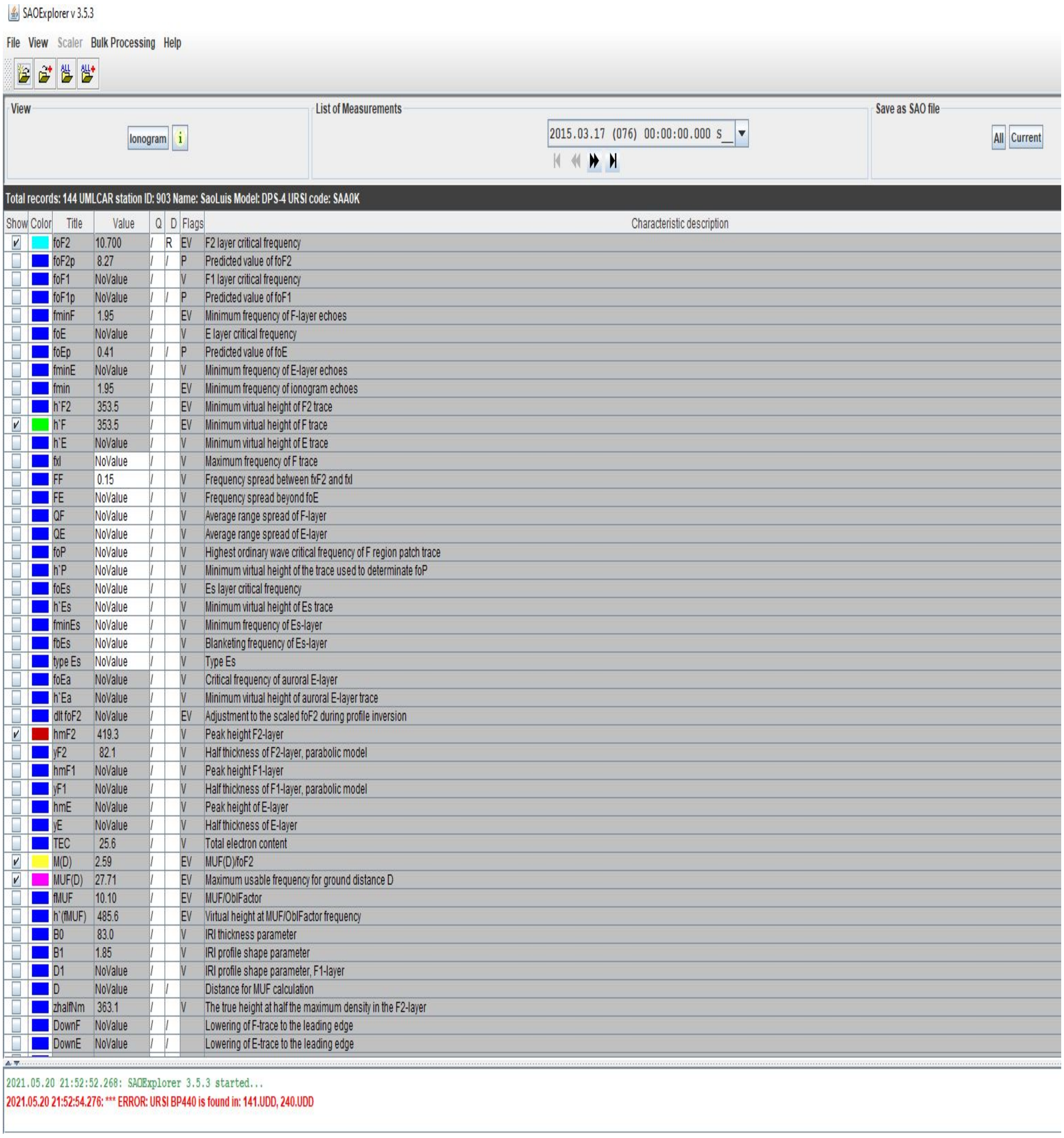

2015.03.17 (076) 00:00:00.000 s

Total records: 144 UMLCAR station ID: 903 Name: SaoLuis Model: DPS-4 URSI code: SAA0K

Show	Color	Title	Value	Q	D	Flags	Characteristic description
☑	🟦	foF2	10.700	/	R	EV	F2 layer critical frequency
☐	🟦	foF2p	8.27	/	/	P	Predicted value of foF2
☐	🟦	foF1	NoValue	/		V	F1 layer critical frequency
☐	🟦	foF1p	NoValue	/	/	P	Predicted value of foF1
☐	🟦	fminF	1.95	/		EV	Minimum frequency of F-layer echoes
☐	🟦	foE	NoValue	/		V	E layer critical frequency
☐	🟦	foEp	0.41	/	/	P	Predicted value of foE
☐	🟦	fminE	NoValue	/		V	Minimum frequency of E-layer echoes
☐	🟦	fmin	1.95	/		EV	Minimum frequency of ionogram echoes
☐	🟦	h`F2	353.5	/		EV	Minimum virtual height of F2 trace
☑	🟩	h`F	353.5	/		EV	Minimum virtual height of F trace
☐	🟦	h`E	NoValue	/		V	Minimum virtual height of E trace
☐	🟦	fxI	NoValue	/		V	Maximum frequency of F trace
☐	🟦	FF	0.15	/		V	Frequency spread between fxF2 and fxI
☐	🟦	FE	NoValue	/		V	Frequency spread beyond foE
☐	🟦	QF	NoValue	/		V	Average range spread of F-layer
☐	🟦	QE	NoValue	/		V	Average range spread of E-layer
☐	🟦	foP	NoValue	/		V	Highest ordinary wave critical frequency of F region patch trace
☐	🟦	h`P	NoValue	/		V	Minimum virtual height of the trace used to determinate foP
☐	🟦	foEs	NoValue	/		V	Es layer critical frequency
☐	🟦	h`Es	NoValue	/		V	Minimum virtual height of Es trace
☐	🟦	fminEs	NoValue	/		V	Minimum frequency of Es-layer
☐	🟦	fbEs	NoValue	/		V	Blanketing frequency of Es-layer
☐	🟦	type Es	NoValue	/		V	Type Es
☐	🟦	foEa	NoValue	/		V	Critical frequency of auroral E-layer
☐	🟦	h`Ea	NoValue	/		V	Minimum virtual height of auroral E-layer trace
☐	🟦	dlt foF2	NoValue	/		EV	Adjustment to the scaled foF2 during profile inversion
☑	🟥	hmF2	419.3	/		V	Peak height F2-layer
☐	🟦	yF2	82.1	/		V	Half thickness of F2-layer, parabolic model
☐	🟦	hmF1	NoValue	/		V	Peak height F1-layer
☐	🟦	yF1	NoValue	/		V	Half thickness of F1-layer, parabolic model
☐	🟦	hmE	NoValue	/		V	Peak height of E-layer
☐	🟦	yE	NoValue	/		V	Half thickness of E-layer
☐	🟦	TEC	25.6	/		V	Total electron content
☑	🟨	M(D)	2.59	/		EV	MUF(D)/foF2
☑	🟪	MUF(D)	27.71	/		EV	Maximum usable frequency for ground distance D
☐	🟦	fMUF	10.10	/		EV	MUF/OblFactor
☐	🟦	h`(fMUF)	485.6	/		EV	Virtual height at MUF/OblFactor frequency
☐	🟦	B0	83.0	/		V	IRI thickness parameter
☐	🟦	B1	1.85	/		V	IRI profile shape parameter
☐	🟦	D1	NoValue	/		V	IRI profile shape parameter, F1-layer
☐	🟦	D	NoValue	/	/		Distance for MUF calculation
☐	🟦	zhalfNm	363.1	/		V	The true height at half the maximum density in the F2-layer
☐	🟦	DownF	NoValue	/	/		Lowering of F-trace to the leading edge
☐	🟦	DownE	NoValue	/	/		Lowering of E-trace to the leading edge

```
2021.05.20 21:52:52.268: SAOExplorer 3.5.3 started...
2021.05.20 21:52:54.276: *** ERROR: URSI BP440 is found in: 141.UDD, 240.UDD
```

SOURCE: Author.

After selecting the parameters, the ionogram icon is clicked on and there is a display of the ionogram, which includes some facilities to manual processing of the data, thus obtaining the profile with the actual altitude of the electron density (n_e). In general, the raw data are manually processed in order to eliminate the noise and obtain a clean ionogram.

Once the raw data are manually processed by taking a proper trace along the first echo, then the ionogram characteristics (plots of the selected parameters versus time) can be viewed, and the data can be saved as a text file.

3.4.2 Ionogram

Data collected by Digisonde are essentially echoes of the signal reflected by ionospheric layers. These echoes are arranged according to their frequency of transmission and reflection time to form the so-called ionograms. The ionogram is a record produced by Ionosondes that shows the variation of the virtual height ($h^{'}$) of reflection of the wave of radio as a function of the frequency (f) of that wave.

Reinisch and Xueqin (1983) states that the measured height is called virtual because the Ionosonde measures the time (t) between the transmission and the reception of the same pulse considering that the wave propagated at the speed light in vacuum (c), thus obtaining the relationship:

$$h^{'}f = \frac{ct}{2} \tag{3.1}$$

The received pulse is called an echo and the virtual height is always greater than the real height, due to the delay suffered by the pulse when propagating in a more dense medium than the vacuum, that is, the speed of wave propagation in the ionosphere is less than the speed of light in a vacuum (c).

Figure 3.5 - Ionogram showing the virtual height of reflection, plasma frequency vs true height.

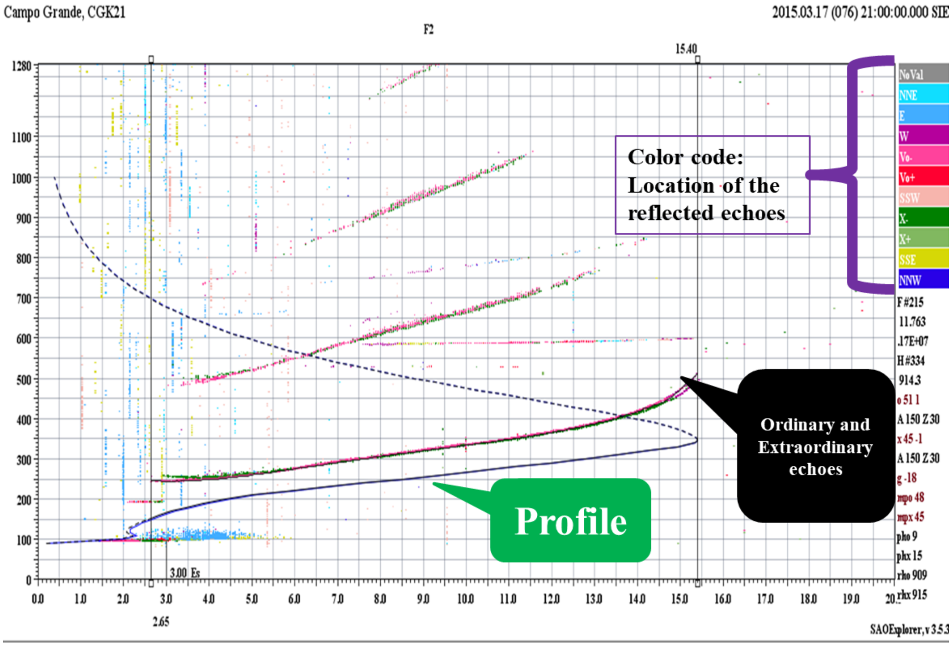

SOURCE: Author.

In the Figure 3.5, there is the first, second and third received frequencies (echoes) of transmission and their corresponding virtual range, as well as the direction of ionospheric echoes. The upwardly curving sections at the beginning of each received frequency are due to the transmitted wave being slowed by underlying ionisation which has a plasma frequency close to, but not equaling the transmitted frequency. The color codes indicates the directional location of the returned echoes; where the top light blue shows the ionospheric reflections from the North-Northeast (NNE), and the bottom deep blue shows the ionospheric reflections from the North-Northwest (NNW), and so on. The echoes are of two colors; red and green which points out the received wave frequencies as ordinary and extraordinary, respectively.

As the conditions of reflection of the ordinary and extraordinary waves are different, each one produces its own pattern $(h' f)$, however, the wave extraordinary is the one that shows the highest critical frequency.

Generally, the color code that appears on the upper right side in Figure 3.5 represents the different directions (south-southwest direction (SSW) or light pink color, south-southeast direction (SSE) or dark yellow color) identified by Digisonde.

3.5 Ionospheric parameters provided by the digisonde

The passage of a radio wave through the ionosphere is influenced by many factors, but predominantly the electron density profile. The electron density is related to the refractive index and some ionospheric parameters.

The ionospheric parameters vary strongly depending on the time of day, season, and location, as well as the solar and geomagnetic activity. Therefore, there is a need to use the continuous monitoring of the propagation medium.

The vertical sounding of the ionosphere is the most validated and reliable approach of measuring the ionospheric parameters. However, there are some disadvantages of sounding as well: the local measurements, large weight and size, high operational expenses and, in the case of using in the communication systems. Nevertheless, this method remains the main source of getting information about the distribution of electron density (KHMYROV et al., 2008; ADEBESIN et al., 2014).

For this particular study research, the five (5) ionospheric parameters, listed in the Table 3.2 are surveyed and analyzed.

Table 3.2 - The description of the ionospheric parameters obtained from the Digisonde for this particular research study.

Parameters	**Description**	**SI Units**
foF2	Critical frequency of the ordinary wave of the F2 layer	MHz
hmF2	Actual peak height of the ordinary wave of the F2 layer	Km
h'F	Minimum virtual height of the trace of the ordinary wave of the F region	Km
MUF(D)	Maximum Usable Frequency for D=3000km	MHz
M(D)	Transmission or Propagation factor	Dimensionless

3.5.1 F2 layer critical frequency (foF2)

The ionospheric parameter foF2 is the maximum radio frequency that can be reflected by the F2 region of the ionosphere at vertical incidence (that is, when the signal is transmitted straight up into the ionosphere). It is the highest frequency at a given ionization density that will be turned down to the Earth when the signal beam is transmitted vertically upward. This frequency is determined by the maximum electron density, and its equation is given by:

$$foF2 = 9\sqrt{N_{max}} \tag{3.2}$$

where: N_{max} = maximum electron density.

In HF radio propagation, foF2 is the limiting frequency at which a radio wave signal is reflected back to Earth's surface by the ionospheric F-layer.

To provide the reliability of the HF communications, it is necessary to estimate such ionospheric parameter as the F2-layer critical frequency - the maximum frequency that can be reflected back to Earth by the ionosphere F2-layer for the vertical incidence.

At any frequency above foF2 value, then the radio wave signal penetrates through the ionospheric F-layer, becoming a transionospheric signal wave.

In summary, it is possible to say that:

- When HF frequency $>$ foF2, then the radio signal transmits through the ionosphere.
- When HF frequency $<$ foF2, then the radio signal is reflected by the ionosphere.
- When HF frequency $=$ foF2, then the radio signal is reflected by the ionosphere.

3.5.2 F2 layer peak height (hmF2)

F2 layer peak height (hmF2) is one of the most important ionospheric parameters characterizing HF signal propagation conditions; as such it is needed for radio frequency planning and spectrum management. Moreover, the Earth-space transionospheric communication can also benefit from the knowledge of the hmF2. An example is the global navigation satellite system which can be improved by mitigating higher order ionospheric propagation effects using the hmF2 information (OBROU et al., 2003).

As is well known, the F2 layer is the most important region of the ionosphere since the ionospheric electron density has its maximum values in this layer. Therefore, hmF2 is one of the key parameters in the determination of the electron density profile.

Oyekola and Fagundes (2012) showed that the temporal and spatial variations of hmF2 depends on the solar activity, daytime and season. However, the peak density height may range from 350 to 500 km at equatorial latitudes. This agrees with the directly obtained and calculated hmF2 ranges of the Sao Luis station in Figure 3.6.

In general, the F-layer peak height varies across the equatorial and low-latitude regions, however, it is highest at the equator zone, as can be seen in Figure 4.8, Figure 4.9 and Figure 4.12 of Chapter 4.

At the equator, hmF2 is largely controlled by the electromagnetic drift, which is upward by day and downward at night. The formation of equatorial trough has something to do with plasma diffusion along magnetic field lines and this was realized during early development of F-layer dynamics (ABDULLAH, 2011).

Additionally, Hoque and Jakowski (2012) have shown that due to regular and irregular variations of the bottomside plasma density closely related to the hmF2 variations, the terrestrial signal transmission may be interrupted or even lost; moreover, the transmission coverage may be affected due to up or down lifting of the ionospheric plasma, changing the hmF2 height.

The hmF2 can be obtained directly from the ionograms, however in practice it can also be calculated using the ionospheric propagating factor [M (D)] which is taken from the ionogram. This propagating factor, also known as M-factor will be discussed properly in subsection 3.5.5.

Karami et al. (2011) and Obrou et al. (2003) used the strong and correlated formula that proved a relation between the peak height and the propagating factor [M (D)], to calculate the hmF2 parameters. This formulation which was presented by SHIMAZAKI (1955) is given by:

$$hmF2 = \frac{1490}{M(D)} - 176 \tag{3.3}$$

Using the propagating factor obtained from ionogram in Equation (3.3), and then we can be able to see the difference in the directly obtained hmF2 and the calculated hmF2. From Figure 3.6, it is seen that the comparison with measured data showed discrepancies when checked with the results calculated from Equation (3.3), this result is in agreement with observation of Rawer and Eyfrig (2004).

Figure 3.6 - Observed and calculated hmF2 of Sao Luis station on the 16^{th}, 17^{th}, and 18^{th} of March 2015.

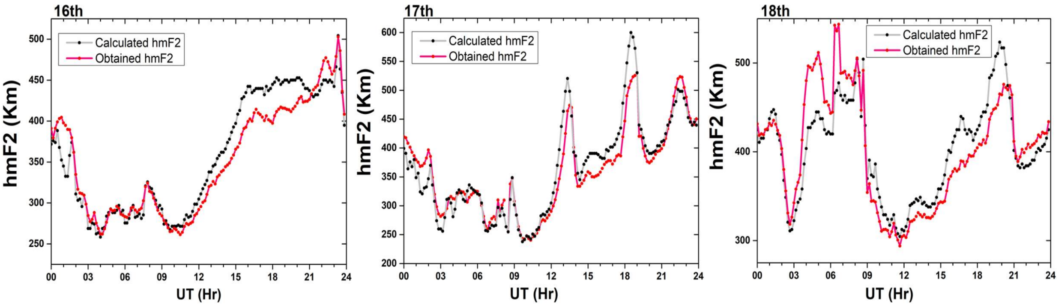

SOURCE: Author.

The discrepancies from the Figure 3.6 show that the calculated hmF2 is higher when the propagating factor increases, and it happened around 12:00 - 21:00 UT for all 3 days. However, the directly obtained hmF2 was greater around 00:00 - 04:00 UT on the 16^{th} and 17^{th},, and then around 03:00 - 08:00 UT on the 18^{th}.

3.5.3 F-layer minimum virtual height (h'F)

The minimum virtual height is the bottom height of the ionosphere that the wave should reach if it was purely reflected instead of being refracted. The height from which total refraction starts is the minimum actual height and is somewhat lower than the minimum virtual height of the layer as seen in Figure 3.7.

According to Canck (2002), the higher the frequency, the higher the virtual height, until we reach the point of maximum electron density of that investigated layer. From that point onward, our wave penetrates the layer and continues its way toward another higher situated layer or, when no more layer are left, finally into space.

Figure 3.7 - Virtual and Actual height of the bottomside ionosphere.

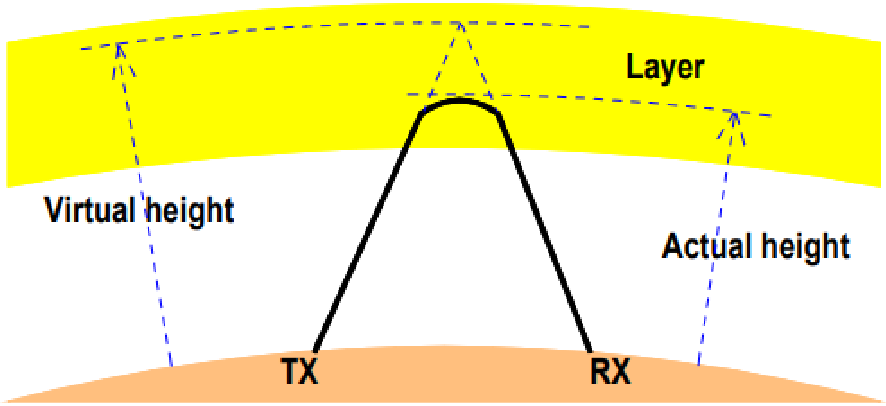

SOURCE: Adapted from Canck (2002).

The minimum virtual height of the F layer at any specified frequency of radiowave signal is the distance in Km that the signal would have traveled at that frequency in half the elapsed time $\left(\frac{T}{2}\right)$ at a speed c. Thus, h'F plays a vital role in how it influences the MUF; this will be discussed and seen properly in the Chapter 4 (Results and Discussion).

3.5.4 Maximum Usable Frequency (MUF)

The MUF is important ionospheric parameter for radio users because of its role in radio frequency management between two locations. And also, MUF helps in the planning of a good communication link.

Souza et al. (2013) defined the MUF as the highest frequency that allows reliable long-range HF radio communication between two points due to ionospheric reflection.

In other words, MUF is the highest frequency that is returned to earth at a given distance. Also, it is the best frequency for communication between any two points under specific ionospheric conditions.

MUF would be used to designate the highest signal frequency for communications that can be used for radio transmission between two points by reflection from the ionosphere at a given time under specific ionospheric conditions, but it can fluctuate continuously because the ionosphere acts as a dispersive medium.

Since HF communications has wide range of application areas, the measurements with the real-time of HF propagation conditions is a key factor of space weather monitoring systems to get satisfactory performance. Hence, it is important to study these parameters that influence propagation in HF communications.

For any communication, there is a maximum usable frequency which is determined by the state of the ionosphere in the vicinity of the reflection points. This implies that, the MUF is reflected from the maximum electron density within a given layer of ionosphere.

At frequencies higher than the MUF, the signal will not reflect, but will transmit (punch) through the ionosphere. Hence, with frequencies higher than MUF, the propagated HF radio wave signals will not reach the receiver.

3.5.5 Ionospheric propagating M-factor [M(D)]

M(D) is also a valuable ionospheric parameter defined as the ratio of the maximum usable frequency (MUF) at a given distance (D) to a given frequennc y (f). Here, it was adopted D=3000 km and f=foF2 (F2 layer critical frequency). M(D) is also called transmission factor or propagation factor.

Zhang et al. (2010) mentions that this parameter, in theory, represents the optimum frequency at which to broadcast a signal that is to be received at a distance of 3000 km.

3.5.6 Relationship between foF2, MUF and M(D) in the equatorial ionosphere

In HF propagation, ionospheric MUF can be calculated by:

$$MUF(D) = foF2 \times M(D) \tag{3.4}$$

where foF2 is the critical frequency of the F2 layer, i.e., the highest frequency that would be reflected by the ionosphere at vertical incidence (KARIM et al., 2019), and M(D) is the propagation factor of layer F2 in which represents the optimal frequency to broadcast a signal received at a hop distance (D) of 3000 km. This hop distance is represented as D and most scientists write M(D) as M(3000)F2.

Souza et al. (2013) stated the simple way to also determine the M-factor using a spherical geometry model. The M-factor [M(D)] obtained with such geometry is given by:

$$M\left(D\right) = \sec\left\{\arcsin\left(\frac{R_E(\cos\varepsilon)}{R_E + hmF2}\right)\right\} \tag{3.5}$$

where R_E is the Earth's radius ($R_E = 6371Km$), and ε is the elevation angle, as can be seen in Figure 3.8. The elevation angle ε is given by:

$$\varepsilon = \arctan\left\{\tan\gamma - \frac{R_E}{\cos\gamma \times (R_E + hmF2)}\right\} \tag{3.6}$$

$$\gamma = \frac{\pi}{2} - \frac{D}{2R_E} \tag{3.7}$$

Now, using the hmF2 which is the F2-layer peak height obtained from the Digisonde data, Equation (3.6) and Equation (3.7) together with Equation (3.5) where $R_E = 6371Km$, $D = 3000Km$ and $\pi = 3.1415$, then we can calculate the M factor using the spherical geometry.

Figure 3.8 - Illustrates the geometry used to calculate M-factor.

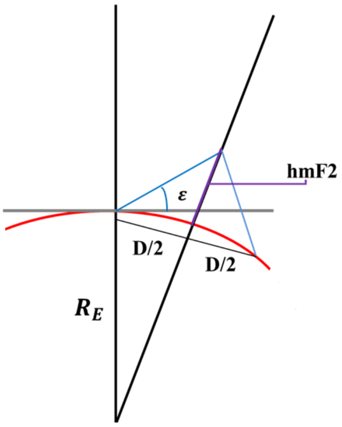

SOURCE: Author.

Due to ionospheric refraction, the aforementioned approach presented is not precise. As such, in order to improve the M-factor calculation, we have considered the ionospheric effects which cause a time delay in the signal propagation and, consequently, an error in M-factor values obtained by only considering spherical geometry. This means that M-factor must be calculated for a virtual hmF2 value ($h'mF2$). However, this $h'mF2$ description will be replaced for only F-region virtual height, so we have that:

$$h'mF2 = hmF2 + \Delta h \tag{3.8}$$

where,

$$\Delta h = \frac{40.3}{(foF2)^2} TEC' \tag{3.9}$$

and TEC', which is the Total Electron Content below the peak height of F2 layer, can be obtained from the ionogram as well.

Using Equation (3.8) and Equation (3.9) into Equation (3.5), then we get that:

$$M(D) = \sec\left\{\arcsin\left(\frac{R_E\left(\cos\varepsilon_0\right)}{R_E + h'mF2}\right)\right\} \tag{3.10}$$

in which, ε_0 is the new elevation angle for any radiowave signal that is reflected at the virtual hmF2 $\left(h'mF2\right)$.

Figure 3.9 - Illustrates the geometry used to calculate M-factor with Δh.

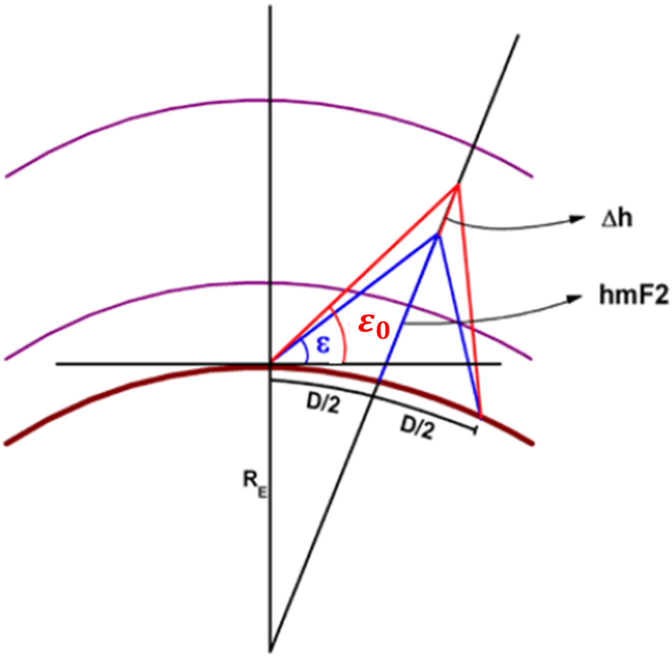

SOURCE: Adapted from Souza et al. (2013).

Souza et al. (2013) states that this new approach seen in Figure 3.9 involving the use of Equation (3.10) works for D=3000Km.

4 RESULTS AND DISCUSSION

In this chapter, the results of this research work are shown. The ionospheric response to an intense geomagnetic storm in March 2015 is studied and discussed. For this purpose ionospheric parameters variation taken from sounding by Digisondes installed at the equatorial region São Luis (SL) and at around the south crest of EIA, in Campo Grande (CG) were analyzed.

4.1 Solar and geomagnetic activity in March 2015

The variations in solar and geomagnetic activity that occurred for the month of March 2015 will be reviewed in this section. The Figure 4.1 presents the solar parameter F10.7, the geomagnetic index, Dst, and the auroral activity index, AE, for the period of March 2015, in order to show the level of solar activity and the geomagnetic disturbance level in the month.The small red rectangles show the 5 quietest days, while the blue rectangle shows the whole storm interval.

Figure 4.1 - Solar and geomagnetic indexes variation during March 2015. F10.7 is the solar flux index, in SFU, where $SFU = 10^{-22} W m^{-2} Hz^{-1}$; Dst is the Disturbance Storm time index and AE is the auroral electrojet index. The red rectangles show the 5 quietest days (5QD), and the blue rectangles show the storm interval.

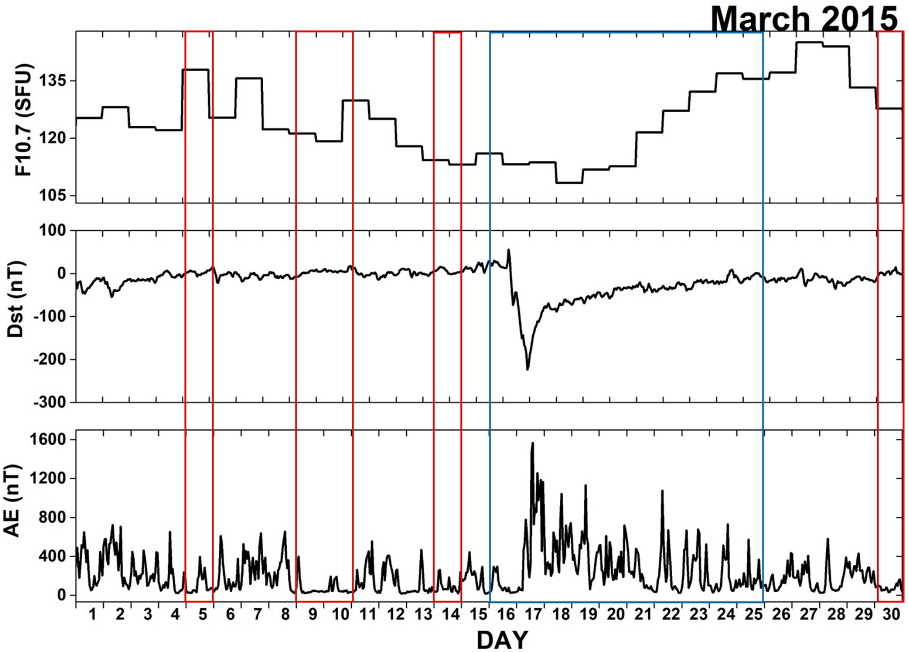

SOURCE: Author.

Figure 4.1 shows from top to bottom panel, solar and geomagnetic indexes for March 2015. On top panel is shown the solar flux index, F10.7, which present typical values of moderate solar activity. The middle panel shows the Dst index. The deep decrease in Sym H represents the intense geomagnetic storm on March 17^{th}. The bottom panel presents the auroral electrojet index, AE (nT) variation.

The solar activity presented typically moderate values between 110 and 150 SFU. And, it may be noted that for this particular month, the solar activity started high and slowly decreased in average along the month but presented a peak on the 27^{th} when solar index F10.7 reached about 150 SFU (where $SFU = 10^{-22} W m^{-2} Hz^{-1}$).

It can also be seen that the period had relatively high auroral activity shown by AE index peaks of 1600 nT. During this AE fluctuations, the Dst index show highly negative values characterizing the occurrence of geomagnetic storms. The first super geomagnetic storm of solar cycle 24 happened on 17^{th} March (Dst = - 223 nT), popularly known as Saint Patrick's Day storm.

Figure 4.2 shows the variation of the interplanetary and geomagnetic indices during this entire month of study. From top to bottom the Figure 4.2 shows the variations of the interplanetary magnetic field intensity, |B|; its components B_x, B_y, and B_z; the solar wind velocity, Vsw; the proton density of the solar wind, Np; the interplanetary electric field, E_y; the auroral geomagnetic index, AE; and the symmetric-H geomagnetic index, SYM/H.

According to Wu et al. (2016), the solar event (a C9.1/1F flare (S22W25)) and a series of type II/IV radio bursts) reached the Earth's magnetosphere on the 17^{th} of March in the form of shock wave in the solar wind (a stream of charged particles emanating from the Sun) hitting the Earth's magnetic field, thus signaling the arrival of Interplanetary Coronal Mass Ejection (ICME).

Generally, all the parameters of Figure 4.2 show some weak variations along the month. However, it is around the middle of March that a huge disturbance can be noted in all the interplanetary parameters with correspondent variations in the geomagnetic indices. These variations are associated with the huge geomagnetic disturbance event, known as the St Patrick's Day storm as mentioned earlier, was caused by the solar event that happened on 15^{th} March 2015.

Using the SYM/H index, which is the bottom panel of Figure 4.2, we can see that the initial phase of the storm was on the 17/03, and the main phase was also on the 17/03, while the recovery phase lasted for 8 days from 18/03 till on the 25/03.

The main phase of this large intense geomagnetic storm occurred on St. Patrick's

Day, which was the 17^{th} of March 2015, with the SYM/H index reaching its minimum excursion of -233nT and the AE reached a peak greater than 2000nT.

From Figure 4.2, it can be seen from the panel 5 (solar wind velocity) that the geomagnetic storm occurs when there is a large sudden increase in the solar wind speed accompanied by a large southward B_z. As can be seen that when the Vsw suddenly increased to around 600km/s, the B_z turned southward with a large negative value of almost -30nT.

Figure 4.2 - Variations of the interplanetary and geomagnetic indices during the month of March 2015. From top to bottom panels: Interplanetary magnetic field in GSM coordinate system: |B| and its components B_x, B_y B_z, (nT); Solar wind speed, Vsw (km/s); Proton density, NP (1/cm-3); Interplanetary Electric Field, E_y (mV/m); Auroral electrojet index, AE (nT), and the 1-min intensity of ring current index, SYM/H (nT).

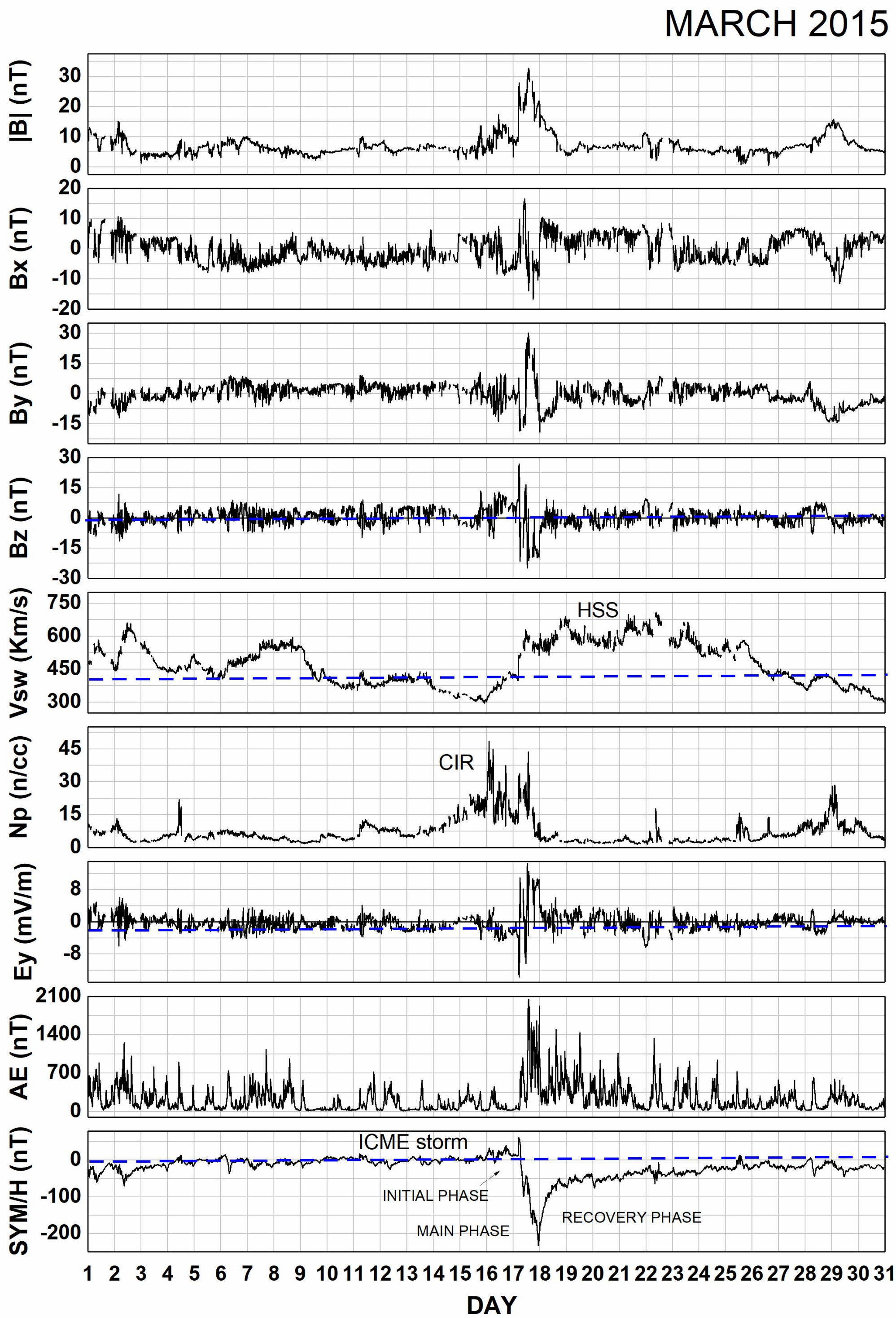

SOURCE: Author.

It can be seen that during the main phase of the storm, the interplanetary magnetic field reached values above 30 nT and the components B_x, B_y and B_z showed large oscillations between negative and positive values. We can notice that on 17^{th} of March, the vertical component of the magnetic field, B_z, presented negative values, the solar wind velocity drastically reduced, while the electric field, E_y, had large fluctuations. The southward direction of the IMF B_z component, indicated by its negative values, is the main key for the magnetic reconnection, that is the main mechanism of the geomagnetic storms.

It can be seen from panel 5 that there are different speeds of the solar wind, (GOSLING; PIZZO, 1999). These different solar wind velocity can become radially aligned to form a compressive interaction regions as a result of spatial variability in the coronal expansion and solar rotation. The compression regions formed are known as Corotating Interaction Regions (CIRs). The CIR can result in particle density enhancement and interplanetary magnetic field (IMF) strength increases preceding onset of High Speed Stream (HSS) (GOSLING; PIZZO, 1999; VRŠNAK et al., 2007).

As the HSS begins to arrives, solar wind speed increases drastically, while proton density decreases simultaneously, as seen in panel 5 and 6 of Figure 4.2. After the passage of the CIR and upon transition into the HSS flow, it is seen that the overall IMF strength normally begin to slowly weaken.

For the most part, the Figure 4.2 demonstrates that during the geomagnetic storm event, there were accompanied abrupt changes in the solar wind speed and proton density and in the amplitude of the interplanetary magnetic field (IMF) B_x, B_y, and B_z components. As known by Astafyeva et al. (2017), the main cause of geomagnetic disturbances (substorms and storms) is the southward directed IMF B_z component, which causes the reconnection with the Earth's magnetic field lines. After the magnetic reconnection (southward direction of B_z), there was an increase in the ring current, inducing a magnetic field contrary to the Earth's horizontal field, causing the SYM/H index to decrease, and AE experienced severe variations. It is believed that the variation of AE is due to the injection of energy in the auroral region.

4.2 Equatorial and low-latitude ionospheric response to Saint Patrick's Day geomagnetic storm

In this section, we analyze the behavior of the equatorial and low-latitude ionosphere during the geomagnetic storm of March 2015. At first, we analyze the plasma frequency, foF2, from the data processing technique explained in Chapter 3, of how the ionospheric parameters are extracted, therefore, the operational activity of the critical frequency (foF2) and MUF during the storm intervals for the two stations could be more clearly observed, as presented in Figure 4.5.

4.2.1 Variation of the critical plasma frequency, foF2 (MHz) and the Maximum Usable Frequency, MUF (MHz) at São Luis, SL and Campo Grande, CG

As mentioned in the subsection 3.5.6 of Chapter 3, foF2 and MUF are related by Equation (3.4). With the purpose of checking the relation, we present the variation of the two ionospheric parameters at the separate latitudinal stations of SL and CG during the geomagnetic storm interval (the day before the storm, 16^{th}, the main phase day of the storm, 17^{th}, and the first recovery day of the storm, 18^{th} to 25^{th}).

The foF2 values for the both stations are analyzed, so as to see the dissimilarity in this parameter for the stations. Figure 4.3 presents the variation of foF2 at São Luis and Campo Grande during the geomagnetic storm interval (from 16^{th} to 25^{th} March). At the top panel, the foF2 variation is presented with the five quiet days average (5QD) at São Luis, the middle panel shows the foF2 and its 5QD curves at Campo Grande, and the bottom panel present the SYM/H variation for the period.

Figure 4.3 - foF2 variation at São Luis and Campo Grande the two stations during the storm interval.

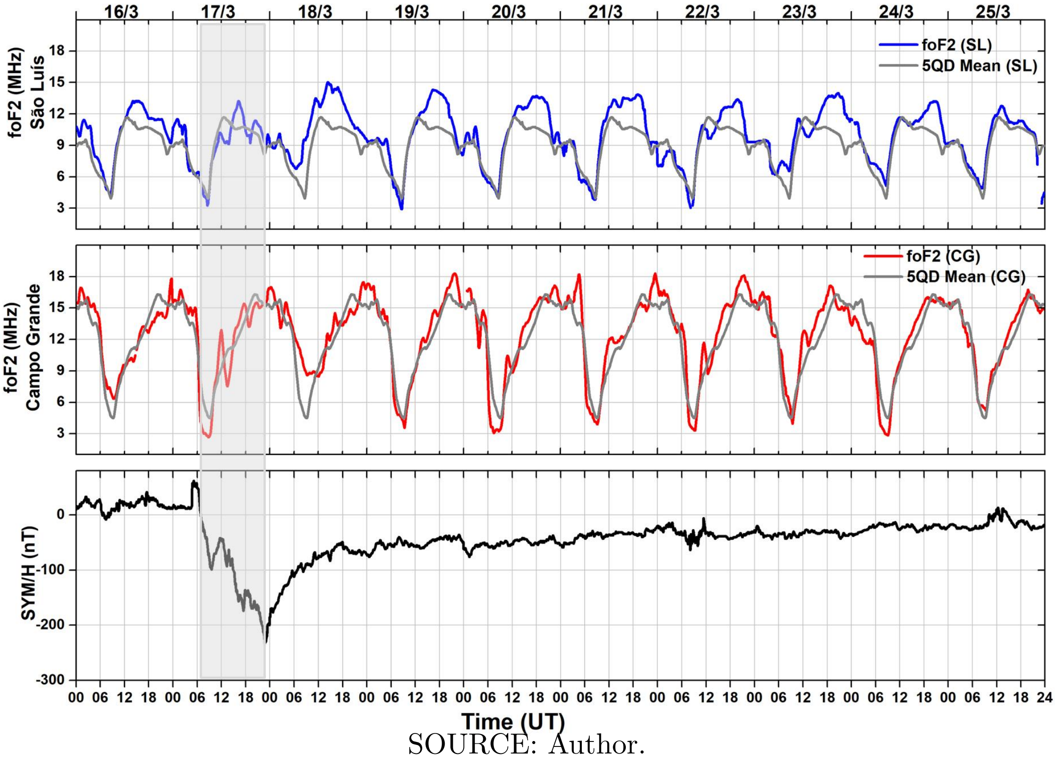

SOURCE: Author.

Figure 4.3 shows that over Campo Grande the average 5QD values are usually within the range of 4MHz – 17MHz, while within the range of 3MHz – 12MHz at São Luis station. The values of the storm intervals foF2 (blue line) are much higher than the mean 5QD foF2 (gray line) at the São Luís (equatorial station). Whereas, at the Campo Grande (low-latitude station), values of the storm intervals foF2 are almost same with the mean 5QD value. We can also find that generally, the foF2 values at Campo Grande station are larger than that at São Luís station.

Additionally, it is shown that the values of the storm intervals foF2 (blue line) are much higher than the mean 5QD foF2 (gray line) at SL. Whereas, at CG, the values of the storm intervals foF2 are almost the same as the mean 5QD value.

We can also see that generally, the foF2 values at CG are larger than that at SL. This is expected since the fountain effect transfers plasma from equatorial region to the EIA region. It is relevant to be noted that some oscillations of this ionospheric parameters at these two stations are out of phase, which is due to time zone difference between them that is ~ 40 minutes.

Similarly, the MUF values for the both stations are examined as well, so as to also see the dissimilarity in the MUF for the stations. The Figure 4.4 presents the variation of MUF at SL and CG during the geomagnetic storm interval (from 16th to 25th March). At the top panel, the MUF variation is presented with the five quiet days average (5QD) at Sao Luis, the middle panel shows the MUF and its 5QD curves at Campo Grande, and the bottom panel present the SYM/H variation for the period.

Figure 4.4 - Variation in MUF for the two stations during the storm interval.

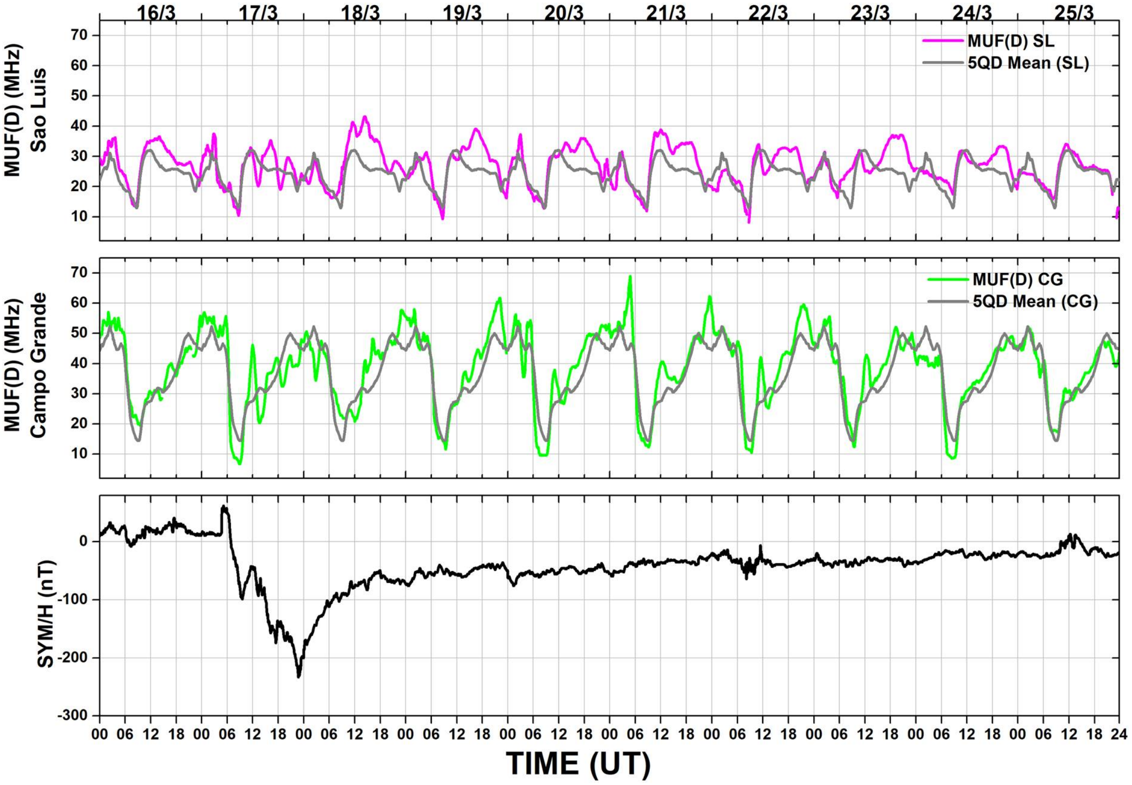

SOURCE: Author.

It can be seen that at the Campo Grande station, the MUF value for 21st March, 2015 during the period after midnight and before dawn 01:00-05:00LT (04:00-08:00UT), is much higher than the value of MUF at the São Luís equatorial station. This particular abnormality is similar to that which occurred on the 18th March, 2015 during the period of pre-dawn till before sunset 08:00-20:00UT (05:00-17:00LT).

Figure 4.4 shows that over Campo Grande, the average 5QD values are usually within the range of 15MHz – 52MHz, while within the range of 12MHz – 33MHz at São Luis station. The São Luís station morning variations of the MUF have lower values compared to the afternoon and evening hours MUF variations. It is also shown that the values of MUF for the interval are very much higher than the mean 5QD MUF at the São Luís. Whereas, at the Campo Grande, the interval’s MUF values are almost same with the mean 5QD’s value.

Overall, it is seen that the MUF values at CG are larger than that at SL. This difference in the MUF values is due to the Electrodynamics (Equatorial Ionization Anomaly, EIA) of the equatorial and low-latitude ionosphere.

Furthermore, the variation of foF2 and MUF are presented. Figure 4.5 shows the variation of the foF2 (red curve) and MUF (magenta curve) from 16th to 18th March at São Luis (top and second panels) and Campo Grande Stations (third and fourth panels) respectively with their reference mean 5QD, as well as the SYM/H index (black curve of the bottom panel).

For both sides of the figure, at the top panel the foF2 variation is presented with the mean five quietest days (5QD), the middle panel shows the MUF and its 5QD curves, and the bottom panel presents the SYM/H variation for the period.

Figure 4.5 - foF2 and MUF variations during the geomagnetic storm in March 2015, over São Luís and Campo Grande stations.

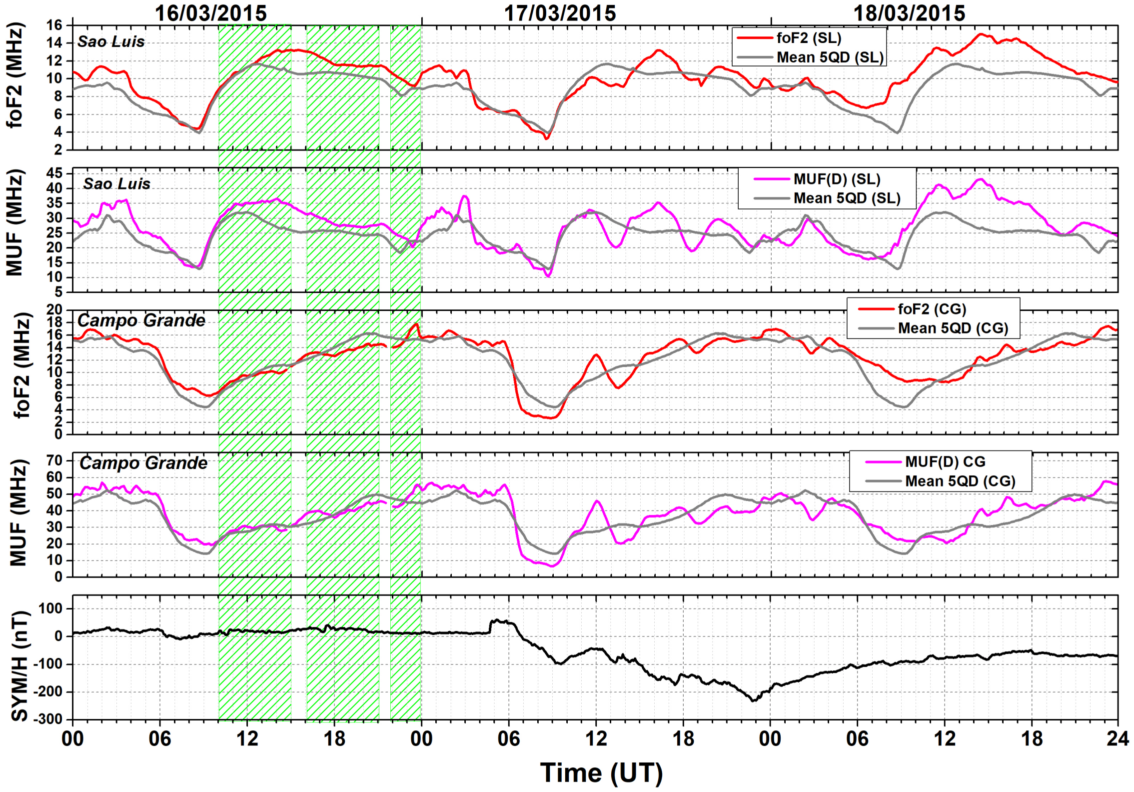

SOURCE: Author.

From Figure 4.5, it is observed that foF2 and MUF values are higher in the morning, 10:00 - 15:00 UT (07:00 - 12:00 LT), and afternoon, 16:00 – 21:00 UT (13:00 – 18:00 LT) than in evening, 22:00 – 24:00 UT (19:00 – 21:00 LT).

The observations from the São Luis station (top and second panels) clearly indicates that for the interval of these 3 days, the following holds: lowest foF2 value around

3-5 MHz in the early morning 08:00-10:00 UT (05:00-07:00 LT), increasing to about 10-14 MHz in the afternoon 16:00-20:00 UT (13:00-17:00 LT) until pre-sunset, and finally decreasing to around 9-11 MHz at post-sunset until pre-sunrise. On the other hand, lower MUF value around 8-13 MHz in the morning 08:00-12:00 UT (05:00-09:00LT), increasing to about 19-37 MHz in the afternoon 16:00-20:00 UT (13:00-17:00 LT) until pre-sunset, and finally decreasing to around 16-20 MHz at post-sunset until pre-sunrise.

However, from the Campo Grande station presented in the third and fourth panels, the foF2 and MUF variations show a trend almost similar to that of the Sao Luis station, with the foF2 and MUF values increasing from early morning to afternoon until pre-sunset, and finally decreasing at post-sunset until pre-sunrise. Only that the frequency values are higher for the CG station.

These results allow us to get an understanding that the foF2 and MUF variations for the both stations have higher values during the early morning until afternoon.

In view of ascertaining the particular time for frequency peak of the two parameters at the both stations, the Table 4.1 presents the specific time at which the foF2 and MUF occurred for the 3 individual days.

Table 4.1 - Peak Time for foF2 and MUF at both stations.

	Sao Luis (SL)				Campo Grande (CG)			
	UT(Hr)	foF2(MHz)	UT(Hr)	MUF(MHz)	UT(Hr)	foF2(MHz)	UT(Hr)	MUF(MHz)
16/03/2015	14 : 00	15	14 : 00	36	01 : 00	18	02 : 00	59
17/03/2015	16 : 00	13	03 : 00	37	02 : 00	16	01 : 00	57
18/03/2015	14 : 00	15	14 : 00	43	23 : 00	17	23 : 00	58

Another observation from Figure 4.5 is that at both equatorial and low-latitude stations, the ionospheric parameters experienced significant oscillations in their values during the main phase and the beginning of the recovery phase of the storm (17^{th} and 18^{th}), their variation presented slightly high values than their reference mean 5QD.

For the purpose of investigating the effects of the geomagnetic storm on the parameters, the foF2 and MUF of the storm intervals was compared to their mean 5QD. It is observed that at São Luis, on the 16^{th} from 12:00 to 23:00 UT, on the 17^{th} from 14:00 to 17:00 UT, and 18^{th} March, from 10:00 to 22:00 UT, the foF2 and MUF are higher than their reference mean 5QD values. The percentage deviation in the increase of the parameters is calculated using the following approach:

$$\%Deviation = \frac{(CPV) \times 100\%}{HPV} - \frac{(CMV) \times 100\%}{MV} \tag{4.1}$$

where;

CPV is the Current Parameter Value,

HPV is the Highest Parameter Value,

CMV is the Current Mean 5QD Value, and

HMV is the Highest Mean 5QD Value.

Using Equation (4.1), the maximum percentage deviation can be obtained. The obtained percentage deviations are shown in Table 4.2.

Table 4.2 - Percentage maximum deviations of foF2 and MUF from their reference mean 5QD for different phases of the storm.

	Initial phase		Main phase		Recovery phase	
	foF2 (in %)	MUF (in %)	foF2 (in %)	MUF (in %)	foF2 (in %)	MUF (in %)
SL	12	23	14	25	12	24

It is worthy to note that at São Luis station, on the 17th the MUF experienced two significant decreases from its reference mean 5QD around 13:00 UT and 18:00 UT. These decreases in values are associated with the ionospheric phenomenon, Prompt Penetration Electric Field (PPEF), that is discussed in detail in section 4.5. On the other hand, at Campo Grande, there was no significant variations from the ionospheric parameters and their reference mean 5QD values for the 3 days shown in Figure 4.5.

4.3 Maximum Usable Frequency – observed and calculated

In subsection 3.5.6 of Chapter 3, where we discussed how to obtain MUF using the approach of the propagating factor (M-factor) calculation, as reported by Souza et al. (2013), whereby there is consideration of the effect of Earth's spherical geometry, as shown in Figure 3.9.

In this work the same method was employed in order to correct the MUF considering the spherical geometric effects as well as effects of the geomagnetic storm. The Earth's spherical geometry was considered with a view to evaluate the impact of F2 layer uplift due to geomagnetic disturbances. The first calculation employs the algorithm suggested by Souza et al. (2013) for quiet days, where the hmF2 of the mean 5QD values presented in subsection 3.5.2 was used. After the process of the M-factor calculation considering the spherical geometry, we introduced the disturbed hmF2 in order to see the geomagnetic storm effect on MUF keeping the disturbed foF2 to allow a relative analysis.

Both the hmF2 of the mean 5QD and the disturbed hmF2 were used in Equation (3.8) and (3.10), this implies that the spherical geometry shown in Figure 3.9 and the ionospheric effect corrections were taken into account.

The calculated M-factor values were then used in Equation (3.9) to obtain two separate corrected MUF values (calculated MUF using mean 5QD hmF2 and calculated MUF using disturbed day hmF2). The two calculated MUF values are plotted for comparison with the disturbed day (16^{th}, 17^{th}, and 18^{th}) MUF and the mean 5QD MUF. These comparison will allow us understand the consequence of the upward lift (increase in elevation angle), shown in Figure 3.9, thus pointing towards the spherical geometry of the Earth.

Figure 4.6 shows the MUF variation for the equatorial region São Luis for the day before the storm, March 16^{th} (top panel), the main phase of the storm, March 17^{th} (middle panel), and the first day of the recovery phase, March 18^{th}. At the top panel it is presented the MUF for day 16^{th}, the mean 5QD MUF, and the two calculated MUFs (using mean 5QD hmF2 and hmF2 for day 16^{th}). The middle panel shows the MUF for day 17^{th}, the mean 5QD MUF, and the two calculated MUFs (using mean 5QD hmF2 and hmF2 for day 17^{th}). Finally, the bottom panel displays the MUF for the day 18^{th}, the mean 5QD MUF, and the two calculated MUFs (using mean 5QD hmF2 and hmF2 for day 18^{th}).

Figure 4.6 - Observed and Calculated MUFs at Sao Luis station for $16^{th}, 17^{th}$, and 18^{th} March 2015.

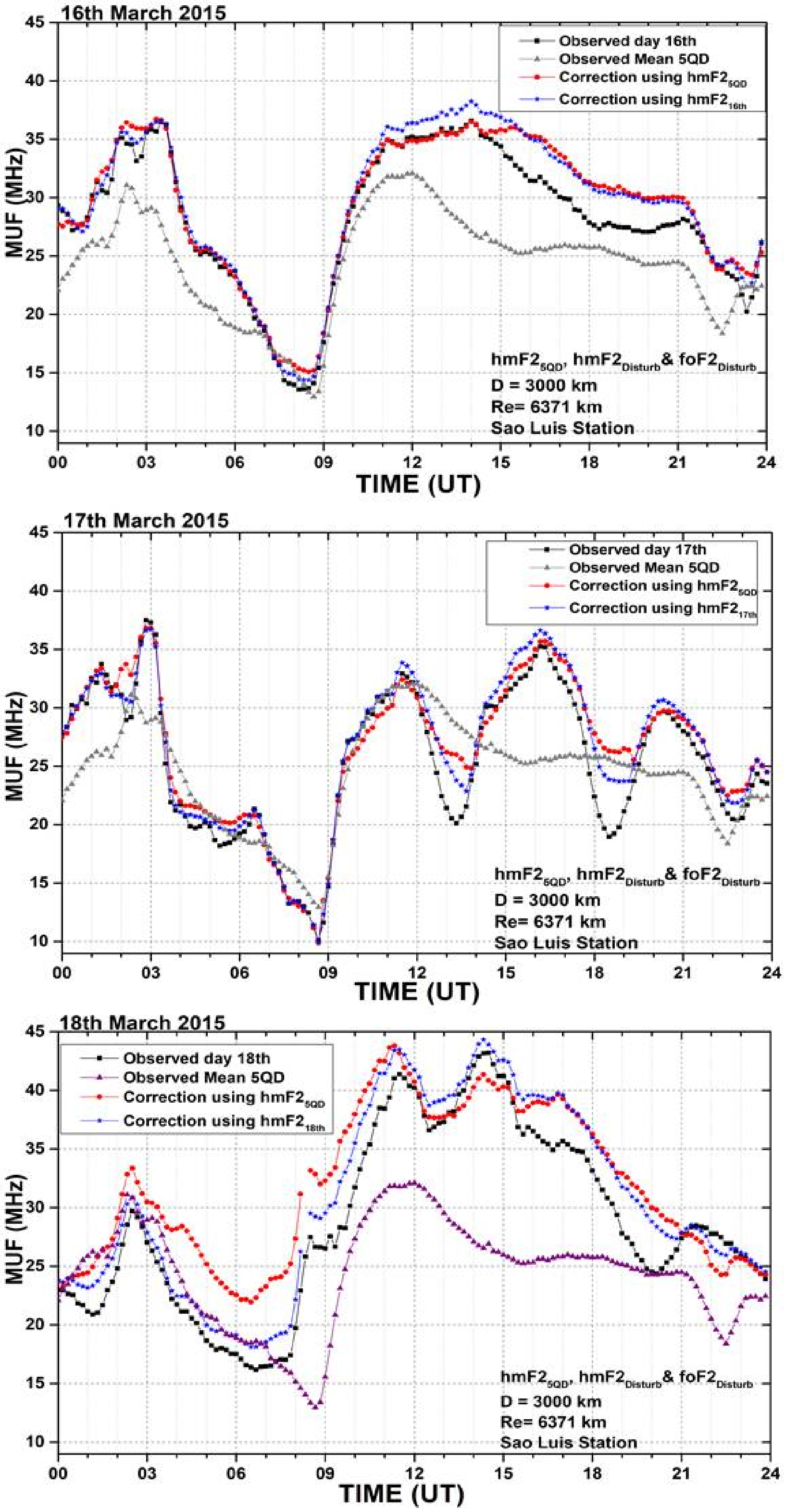

SOURCE: Author.

It is observed that the calculated MUF for the quiet day March 16th present a good agreement for almost the time, except for the interval 11:00 to 15:00 UT (08:00 – 12:00 LT). In general, the calculated MUF values are higher than the mean 5QD MUF values. For the main phase of the storm, March 17th, it is observed a deep depletion in the ccalculated and observed MUF at around 13:00 UT and 18:00 UT, i.e., 10:00 LT and 15:00 LT, in comparison to the mean 5QD MUF values. On the other hand, after MUF calculations considering the effects of spherical geometry (blue line) and geomagnetic storm effects on the F-layer peak height, it is observed that the geomagnetic storm decrease MUF in some intervals, but not so much as shown in observed MUF, at around 13:00, 18:00 and 23:00 UT.

One interesting point to be noticed in the middle panel of Figure 4.6 is that the MUFs calculated by applying only the spherical geometry approach show 3 separate significant differences when compared with the directly obtained ionogram data of 17th around 13:00UT, 19:00UT, and 22:30UT. The observed decrease in the directly obtained MUF values during the first two different time intervals (13:00UT and 19:00UT) are believed to be caused by PPEF events as reported by Venkatesh et al. (2017). However, the observed decrease in the directly obtained MUF values during the last time intervals (22:30UT) is associated with PRE occurrence. This particular PRE that occurred on this day is discussed better in Section 4.5.

Finally, the minimum value of all the different forms of MUF was noticed on the 17th of March, which is during the main phase of the geomagnetic storm, as presented in Figure 4.6.

Similarly, Figure 4.7 shows the MUF variation in Campo Grande station: the current day, the mean 5QD MUF and the two calculated MUFs (using mean 5QD hmF2 for spherical geometry calculation and the current day hmF2). The top panel presents the MUF for day 16th, the mean 5QD MUF, and the two calculated MUFs (using mean 5QD hmF2 and hmF2 for day 16th). The middle panel shows the MUF for day 17th, the mean 5QD MUF, and the two calculated MUFs (using mean 5QD hmF2 and hmF2 for day 17th). And the bottom panel displays the MUF for day 18th, the mean 5QD MUF, and the two calculated MUFs (using mean 5QD hmF2 and hmF2 for day 18th).

Figure 4.7 - Obtained and calculated MUF of Campo Grande station on the $16^{th}, 17^{th}$, and 18^{th} of March 2015.

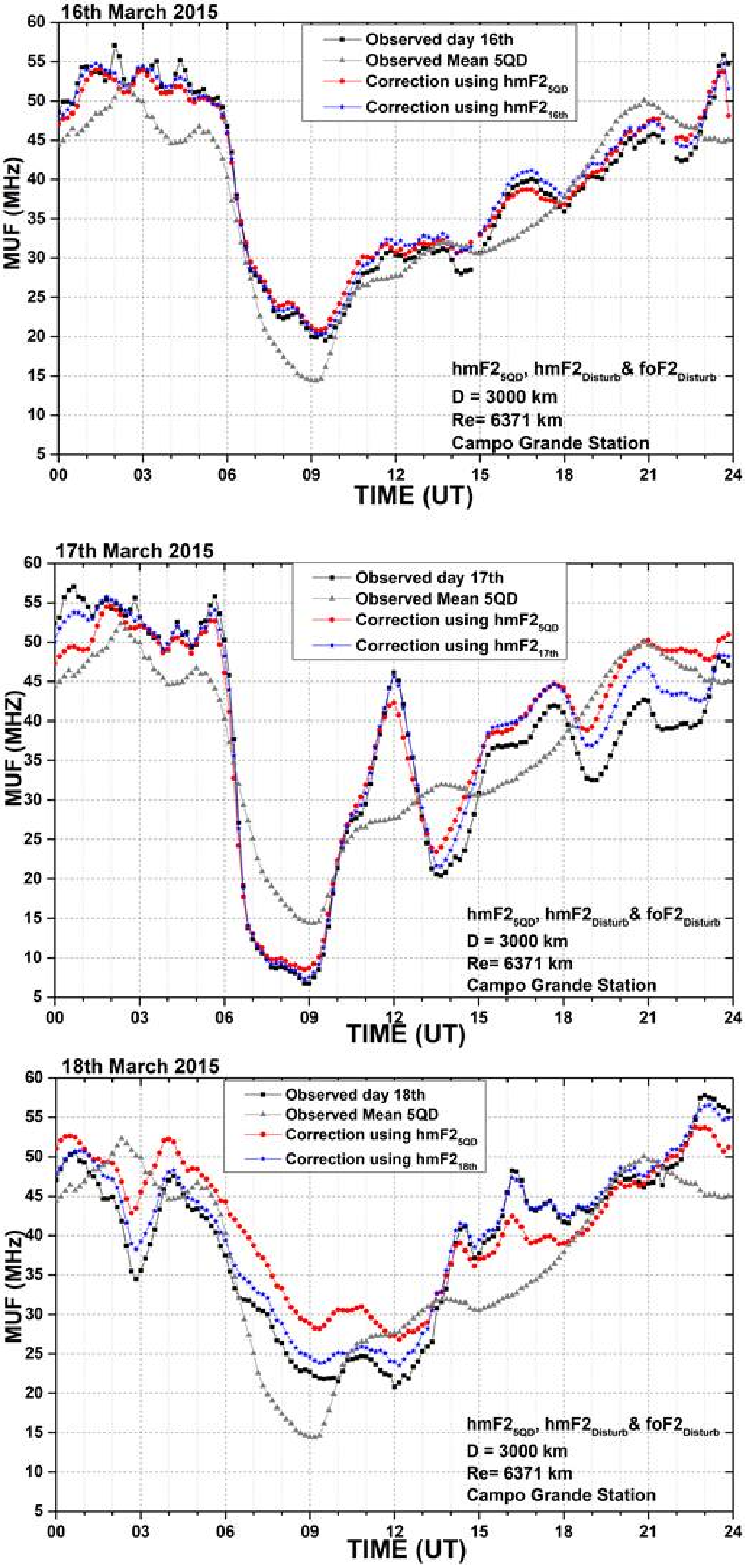

SOURCE: Author.

From Figure 4.7, it can be seen that the MUF values calculated using the ionospheric effect and spherical geometry corrections (blue and red curves) present good agreement with the directly observed MUF of the 3 disturbed days (black curves). On the other hand, there are significant variations from the calculated MUF values (blue and red curves) and the directly observed mean 5QD MUF values (purple curves). The distinct differences are manifested around 11:00 – 23:00 UT (on the 16^{th}), 14:00 – 17:00 UT and 20:00 – 22:00 UT (on the 17^{th}), and finally 08:00 - 24:00 UT (on the 18^{th}). This significant disagreement is believed to be associated with the effect of geomagnetic disturbances.

Also, Figure 4.7 presents that the MUF values calculated using the ionospheric effect and spherical geometry corrections (blue and red curves) shows good agreement with the directly observed MUF of the 3 disturbed days (black curves). However, there are significant variations from the calculated MUF values and the observed disturbed day MUF values (blue, red and black curves) and the directly observed mean 5QD MUF values (purple curves).

In the same manner as the SL results, the minimum value of all the different forms of MUF was noticed on the 17^{th} of March, which is during the main phase of the geomagnetic storm, as presented in Figure 4.7.

After the analysis of the observed and calculated MUF values, the response of the ionosphere to the geomagnetic storm on the day before the storm, main phase of the storm, and the first day of the recovery phase were studied and reviewed in the next section.

4.4 Ionospheric response on the day before the storm commencement

The 16^{th} of March 2015, which is the day before the storm, was examined with the aim of obtaining a finer review of the ionospheric response before the geomagnetic storm, Figure 4.8 shows, from top to bottom panel, the variation of: the ring current index, SYM/H (nT), the vertical component of interplanetary magnetic field, Bz (nT), the interplanetary electric field, Ey (mV/m), the F-layer virtual bottom height, h'F (km), the F-layer peak height, hmF2 (km) as well as the MUF (observed and calculated with mean hmF2) at SL and CG, as well as their mean 5QD.

From Figure 4.8, it can be seen that on this day, the Bz and Ey did not have much significant oscillations, and the SYM/H index experienced no distinct negative incursion.

The F layer height parameters (h'F and hmF2) at SL and CG station showed no substantial difference from their reference mean 5QD values. Typically, the sixth panel showed that over SL, there was two peaks in calculated and observed MUF at 03:30 UT (00:30 LT) and 14:00 UT (11:00 LT). Beside that a minimum is observed at 08:00 UT (05:00 LT). Over CG, there was also two peaks at 02:30 UT (23:30 LT) and 24:00 UT (21:00 LT) and a minimum at 09:00 UT (06:00 LT).

Figure 4.8 - Ionospheric response on the day before the storm.

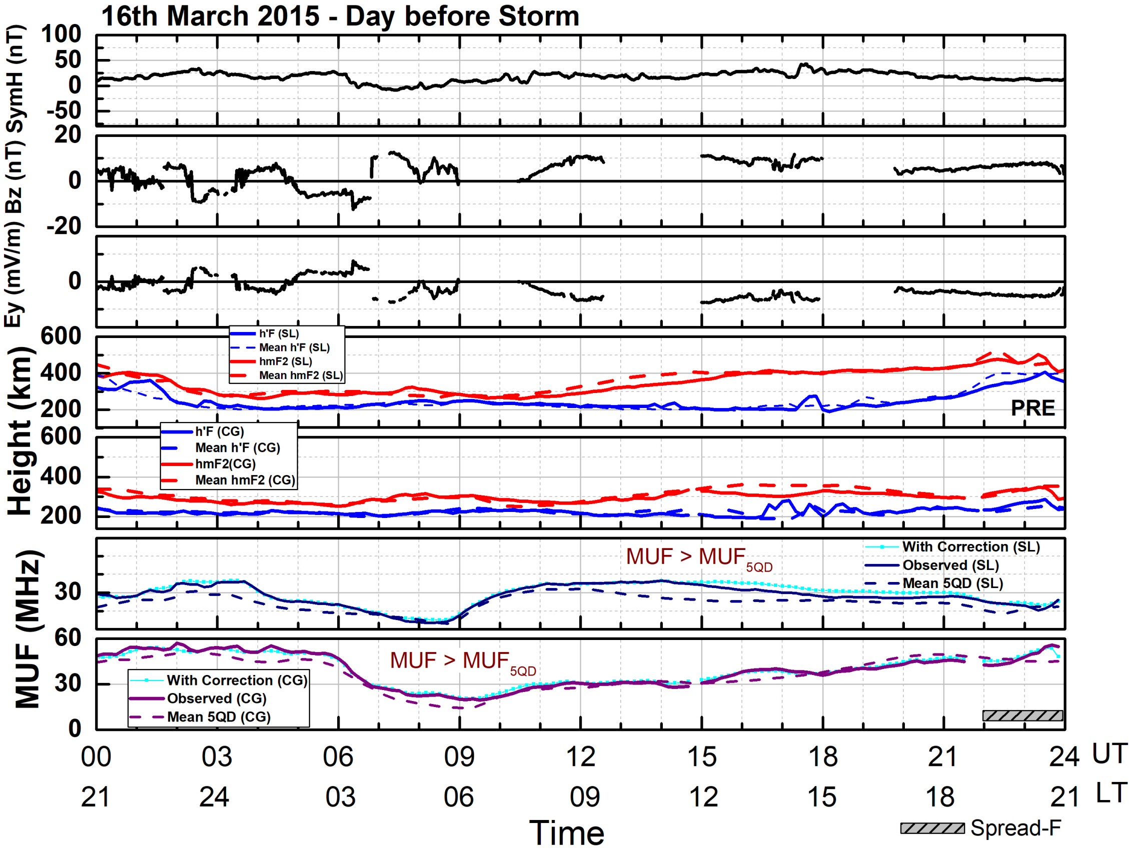

SOURCE: Author.

However, it can also be noticed that the calculated and observed MUF at both stations presented a slight disagreement with their reference mean 5QD MUF values from 00:00 – 06:00 UT (21:00 – 03:00 LT). Meanwhile, at only SL station around 13:00 – 16:00 UT (10:00 – 13:00 LT) the calculated and observed MUF manifested a distinct variation from their reference mean 5QD values.

Finally, it can also be seen that at SL around 22:00UT (19:00LT), the h'F and hmF2 as well as their mean 5QD had an evening uplift. This F-layer uplift observed in h'F at this station during the local evening is the usual PRE at equatorial region, which generally precede the development of plasma irregularities, represented by horizontal dashed gray bar.

4.5 Ionospheric response during the main phase of the Saint Patrick's day storm

As mentioned earlier in Section 4.1, the main phase of the March 2015 occurred on the 17th, which is known as the St. Patrick's Day. The sudden storm commencement was at exactly 04:45UT (01:45LT). For the better evaluation of the response of the ionosphere during this main phase of the geomagnetic Storm, the Figure 4.9 shows the variation of: the ring current index, SYM/H (nT), the vertical component of interplanetary magnetic field, Bz (nT), the interplanetary electric field, Ey (mV/m), the F-layer virtual bottom height, h'F (km) the F-layer peak height, hmF2 (km) as well as the MUF (observed and calculated with mean hmF2) at SL and CG, and their mean 5QD for comparison.

Figure 4.9 - Ionospheric response during the Saint Patrick's Day storm main phase.

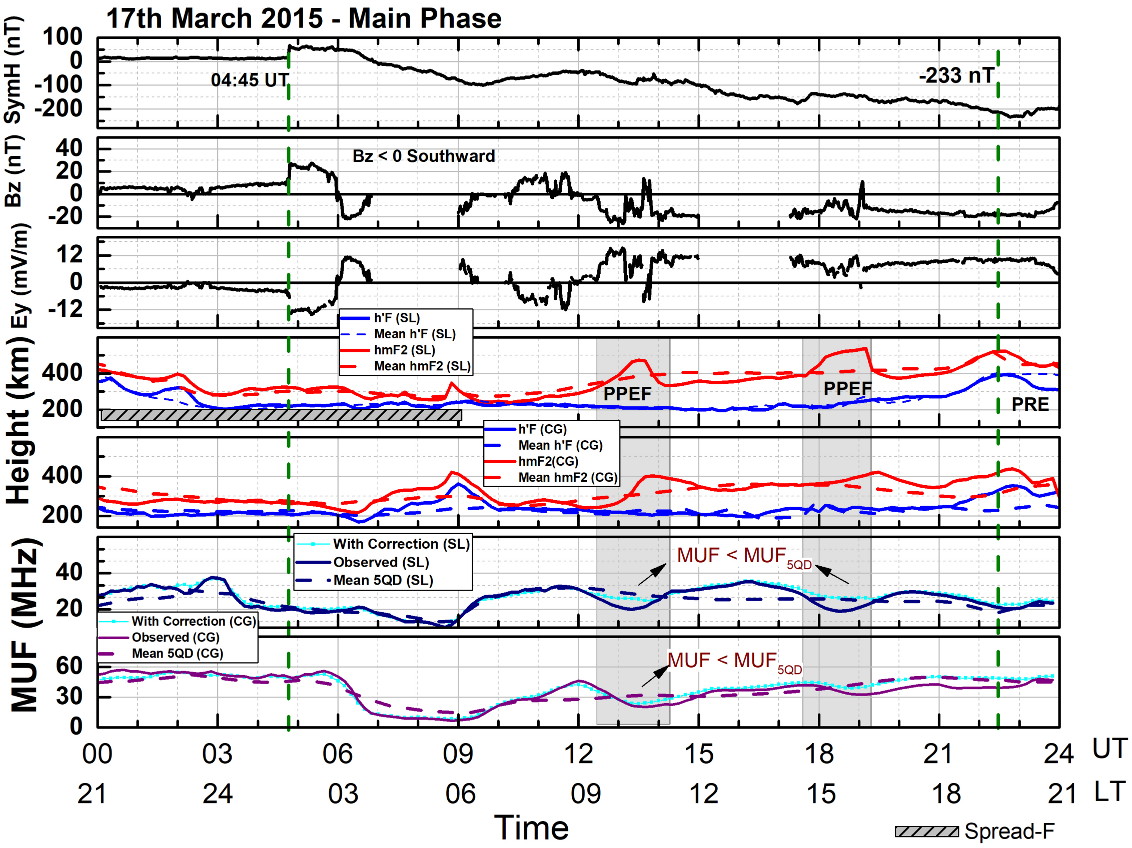

SOURCE: Author.

It is observed from the second and third panels that the main phase of Figure 4.9, the geomagnetic storm began at around 04:45UT (01:45LT) when the vertical component of the interplanetary magnetic field, Bz, turned northward and the Ey having a negative excursion of about 12mV/m. Afterward, at around past 06:00UT (03:00LT), the Bz turned southward and the SYM/H index start decreasing to negative values until 23:00 UT, when it reached its minimum value (end of a long main phase), with no evident ionospheric response during the first hours of the main phase. However, at around 13:00 UT (10:00 LT), it is possible to see a negative excursion of Bz (reconnection processes in course), while Ey turns to positive values (westward dawn-to-dusk electric field).

The ionospheric effects of the southward turning of Bz during this main phase can be seen in the fourth and fifth panels of Figure 4.9. At SL, the F-layer virtual height, h'F does not present any abrupt oscillations or deviation from its mean 5QD, while the F-layer peak height, hmF2 present some uplifts in comparison to its mean 5QD. The first one was observed at around 09:00 UT (06:00 LT) both in SL and CG. However, how this is the interval when the ionization starts increase by the solar radiation, it is possible that it is an apparent uplift. Notice that there are no clear effect on MUF in SL (MUF   mean 5QD MUF), while MUF is lower than the mean 5QD MUF in CG.

Noteworthy is the occurrence of two significant increases of hmF2 (rapid uplifts) from its mean 5QD around 13:00 and 14:00 UT, i.e., at local morning 09:00 and 11:00 LT reaching an altitude peak of 465 km and   520 km, respectively.

The first rapid F-layer peak height uplift suggests the occurrence of enhanced vertical ExB drift at the equatorial region, probably caused by Prompt Penetration Electric Field (PPEF) episodes during periods when Bz < 0 (southward) and Ey > 0.

The second significant hmF2 uplift during the main phase of the St. Patrick's Day storm happened around local noon 18:00 UT (15:00LT) when the Bz turned southward with a strong negative excursion of about -25nT with Ey positive, indicating the second occurrence of PPEF.

It can be seen that at those time periods, the MUF experienced significant decrease in their value compared to its reference mean 5QD MUF (gray line). This deviation was around 25%, which means a potential loss or spurious effects in the radio communication at these times. This implies that during the event of PPEF, the radio communication sector within the station's geographical region will experience loss or fail of radio signal links, because of the lower value of MUF (during the storm compared to its quiet day value), considering that MUF is the highest frequency that allows reliable long-range radio communication between two points.

In order to better infer the MUF variation during a storm, we performed a correction entailing the Earth's spherical geometry effect and the geomagnetic storm effect. It is remarkable that the MUF after calculations presents depletion during the two PPEF episodes, but not so deep as those observed MUF. The deviation of MUF calculated to the mean 5QD MUF during the main phase of this St Patrick's Day storm was calculated using the approach of equation 4.1, and the results are given in Table 4.3.

Table 4.3 - Deviation of MUF calculated to the mean 5QD MUF during the PPEF episodes of main phase of the St Patrick's Day storm.

	Deviation during 1st PPEF (%)	**Deviation during 2nd PPEF (%)**
SL	23	25
CG	7	3

Moreover, we should address that before the ending of the main phase at around 22:30 UT (19:30 LT) at SL, the h'F and hmF2 as well as their mean 5QD had an uplift. It is important to notice that at SL, the F layer dynamics had this singular behavior, which is the F layer evening uplift. This F layer evening uplift is caused by the PRE in vertical drift ExB, which results from the F layer wind dynamo that dominates in the evening. As a result of the eastward zonal electric field Ex and the northward direction of Bz causing the uplift of the plasma (vertical ExB drift reaching maximum).

At the ending of the storm's main phase about 23:00 UT (20:00LT), when the SYM/H index reached its highest minimum value, the Sao Luis h'F reached an altitude of 400 km similar to its mean 5QD reference, which implies that the PRE was not increased or suppressed by the storm.

Finally, it is significant to comment that during the first and second PPEF events, there was manifestation of F3 layer. This F3 layer occurrence will be discussed in the subsection 4.5.1

4.5.1 F3 layer formation

In this work, the ionospheric response to the Saint Patrick 's Storm was analyzed , through the analyzes of important ionospheric parameters taken from ground-based

Digisonde sounding: the critical plasm frequency, foF2, the F-layer virtual and peak heights, h'F and hmF2, as well as the Maximum Usable Frequency, MUF for two representative stations.

During the analysis of parameters extracted from the ionogram, we observed a remarkable occurrence of an additional F-layer, named F3-layer, as shown in Figures 4.10 and 4.11. From these two sequences of ionograms taken from the Digisonde installed at SL, it is possible to observe the formation of F3-layer from 12:40 UT to 13:30 UT (09:40 LT to 10:30 LT) and at 18:00 to 19:10 UT (15:00 LT to 16:10 LT).

The formation of F3 is due, as investigated by Balan et al. (2008) and Balan et al. (1998), to two main factors: the ExB vertical drift, and an equatorward neutral wind. The combined effect of the upward ExB drift and the neutral wind provides a vertically upward plasma drift velocity at altitudes near and above the F2 peak. This vertically upward plasma drift velocity causes the F2 layer peak height to drift upward and form the F3 layer, while the normal F2 layers develop at lower altitudes as a result of the equatorial region electrodynamic effects.

It is asserted by Balan et al. (1998) that the F3 layer forms during the morning to noon (08:30 – 16:30 LT) period in equatorial region (±10 magnetic latitude) as a result of ionization production and equatorial F region electrodynamics. The combination of upward ExB drift and equatorward neutral wind causes the morning-noon period F2 layer to drift upwards. When this F2 layer drifts upward with time to form the F3 layer, then a new layer develops as the usual F2 layer.

In the course of the two PPEF episodes that occurred during the main phase of the St Patrick's Day storm, it is interesting to know that the F2 layer peak height experienced a rapid upward lift. From the ionogram survey shown in Figure 4.10, it is seen that at around 12:40 UT when the peak height of the F2 layer was experiencing an upward lift, it was redistributing at the same time and forming a new layer. The new layer which is F3 layer is seen to be drifting more upward till around 13:30 UT, after which it vanished. As stated by Venkatesh et al. (2017), this redistribution of the usual F2 layer into F2 and F3 layers is a consequence of the enhanced zonal electric field that accompanied the first PPEF episode, thus demonstrating that in the Brazilian equatorial ionosphere, there is substantial augmentation of zonal electric field during the event of PPEF.

Figure 4.10 - Ionogram survey during the first PPEF episode of the St Patrick's Day storm showing the formation of F3 layer.

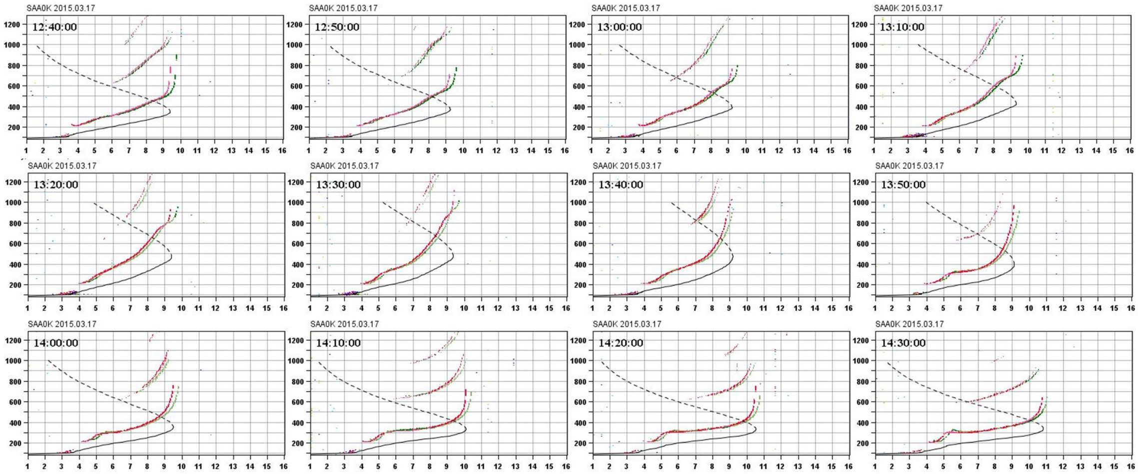

SOURCE: Author.

Figure 4.11 show that the equatorial ionosphere exhibits the same response during the period of the second PPEF event. It is seen that the new layer, which is the F3 layer, drifts extra upward to higher heights during the time interval of 18:10 UT till 19:10 UT when it reached its maximum altitude, and then varnished by 19:20 UT.

Figure 4.11 - Ionogram survey during the second PPEF episode of the St Patrick's Day storm showing the formation of F3 layer.

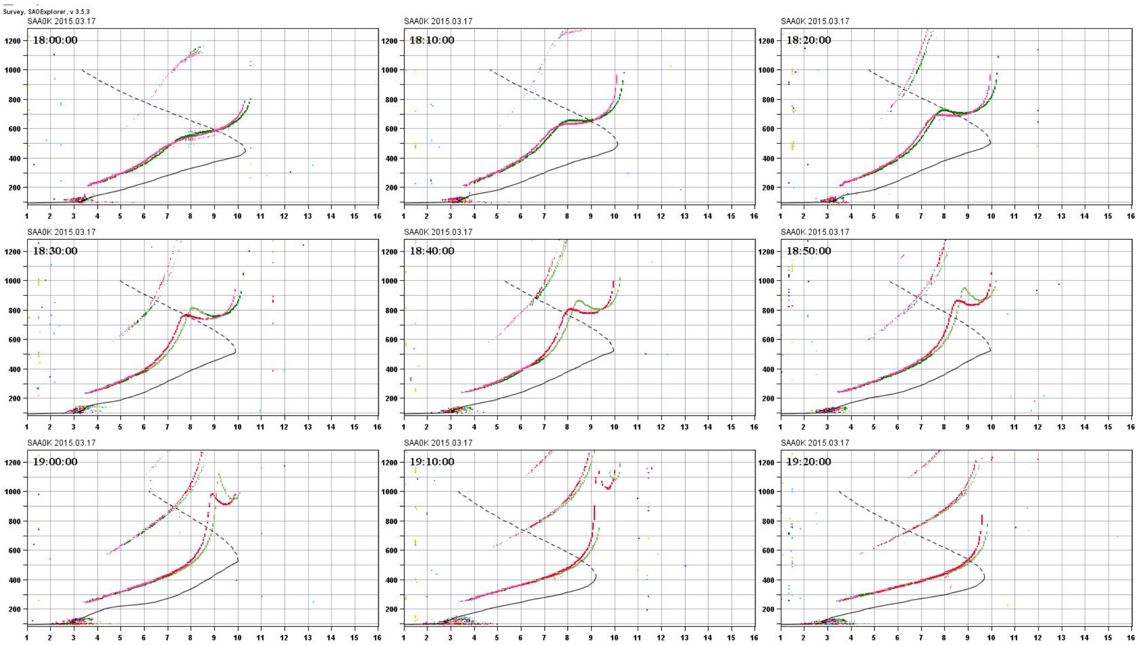

SOURCE: Author.

4.6 Ionospheric response on the 1st day of the storm's recovery phase

In order to have a more complete picture of the ionospheric response to the Saint Patrick Day storm, we analyze what happened after the main phase of the storm. It is remarkable that the recovery phase was unusually long as compared to other ICME-driven storms. Now, to the reason for the long duration of the storm's recovery, from Figure 4.3 and 4.4 it is noticed that the SYM/H was negative until March 25^{th}, when it recovered to its reference quiet day. At the same interval, it possible to see the occurrence an increased solar wind speed (Vsw $\leqslant$ 700 km/s), as seen in panel 6 of Figure 4.2, as well as a Corotating Interaction Region, CIR signature (see the Np increase) at March 17^{th}. Solar parameters, Vsw and Np peak are associated with the occurrence of High-Speed Solar Wind Streams emanated by solar coronal holes. In this studied case, it is possible that the CIR was enclosed in the ICME structure, followed by the HSSWS, which can favor a longer recovery phase.

Figure 4.12 shows the variation of: the ring current index, SYM/H (nT), the vertical component of interplanetary magnetic field, Bz (nT), the interplanetary electric field, Ey (mV/m), the F-layer virtual bottom height, h'F (km), the F-layer peak height, hmF2 (km), as well as the MUF (observed and calculated with mean hmF2) at SL and CG, and their mean 5QD.

Figure 4.12 - Ionospheric response on the first day of the storm's recovery phase.

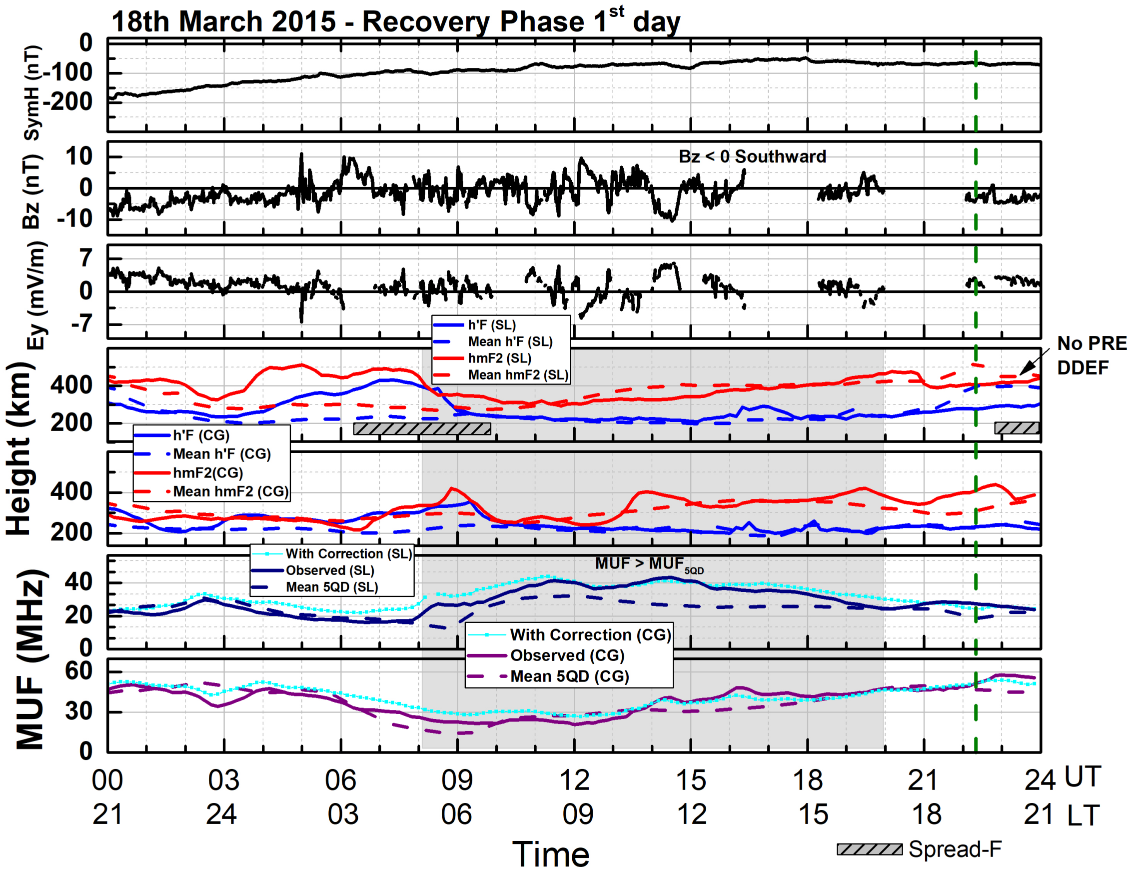

SOURCE: Author.

Around local morning and noon 09:00 to 15 UT (06:00 to 12:00 LT), the Bz and Ey experienced considerable oscillations, although the lower magnitude in comparison to the main phase ones, but not evident PPEF episodes were observed. MUF over SL was higher than its 5QD 09:00 – 18:00 UT (06:00-15:00LT). MUF at CG was higher than its 5QD in afternoon 15:00 – 16:00 UT (12:00-13:00LT). The higher values in SL may be caused by weaker ExB vertical drifts, possibly associated to effects of a Disturbance Dynamo electric field, with inversely electric field polarization, i.e., Ey westward.

From Figure 4.12, one significant event of this particular day is that there is the likelihood of the occurrence of the disturbance dynamo electric field (DDEF) at

SL during post-sunset 22:30 UT (1930LT). These equatorial disturbance dynamo electric fields can clearly be identified by the usual decrease of the storm day h'F and hmF2 from their mean 5QD. However, at that time, there is a mild Bz turned southward and the Ey was positive.

There was no evident occurrence of PRE at 23:00 UT (20:00 LT). Therefore, there is a possibility that this suppression of PRE might be associated with DDEF. However, this effect needs a further investigation using equatorial electrojet data (not included in this work).

5 CONCLUSION

In this Master's dissertation, the extensive investigation of the Brazilian equatorial and low-latitude ionospheric response was carried out to evaluate the behavior of different ionospheric parameters, especially the maximum Usable Frequency (MUF) during the geomagnetic storm of March 2015. This research work was performed as a new contribution to study the equatorial and low-latitude ionospheric response to geomagnetic storms.

The main ionospheric parameters that were extracted from Digisondes such as h'F, foF2, hmF2, M(D), and MUF were analyzed. From the analysis, the relationship between these parameters and how they influence each other during the storm intervals were observed.

From the results, it was seen that the arrival of some solar event on the 15^{th} of March reached the Earth on the 17^{th} of March, causing particle density enhancement and leading to increase in the intense of the IMF.

Additionally, from the results, it was observed that the March 2015 geomagnetic storm was an intense storm with SYM/H index of -233 nT and Dst index of -223 nT, with a very long recovery phase (lasted for 8 days). The day before the storm, the proton density and solar wind speed experienced sudden changes. However, the main phase of the storm had a southward directed IMF Bz component, which leads to magnetic reconnection.

In particular, the variation of foF2 and MUF presented an almost similar trend with high values during the early morning until afternoon. Additionally, there was an observation of the parameters (foF2 and MUF) experiencing significant oscillations during the main phase and the beginning of the recovery phase.

The foF2 and MUF parameters were seen to be generally higher at Campo Grande than at Sao Luis, which is because of the equatorial and low-latitude electrodynamics. And also, the two stations experienced some oscillations in the ionospheric parameters that were out of phase. That can be attributed to the time zone difference between the two regions, which is 40 minutes.

From the results obtained in this work, it was possible to conclude that geomagnetic activity can impact the MUF in some intervals, such as during the PPEF episodes. As PPEF cause F-layer uplift, the equatorial plasma reach higher altitudes and can be transported by means of gravity, diffusion, and pressure gradients to higher latitudes. In this way, the MUF is dependent on the foF2 as indicated by Equation (3.9) and on the F-layer height variation. During a geomagnetic storm, MUF can decrease drastically affecting the HF radio communication for some intervals, as seen during the time intervals of the PPEF episodes. However, this needs further investigation.

In addition, the M(D), which is the propagation factor was calculated to consider the influence of the Earth's spherical geometry and the effect of geomagnetic storm on MUF (FAGRE et al., 2019; LLOSA et al., 2007). The outcome of this particular investigation showed that there was a good agreement between the calculated MUF values on the day before the storm at the Sao Luis region, and also, the corrected MUF values were approximately higher than their reference mean 5QD MUF values.

From the analysis of the observed, calculated MUF, mean 5QD MUF, h'F, and hmF2, it was observed that the ionosphere presented the following responses:

- On the day before the storm commencement, the h'F and hmF2 showed no substantial difference from their mean 5QD values at both stations. Over Sao Luis, two peaks were noticed in the corrected and observed MUF at ∼3:30 UT (00:30 LT) and 14:00 UT (11:00 LT) and a minimum at 08:00 UT (05:00 LT). In the same vein, over Campo Grande, two peaks were also noted to occur in the corrected and observed MUF at ∼2:30 UT (23:30 LT) and 24:00 UT (21:00 LT) and a minimum at 9:00 UT (6:00 LT).
- During the main phase of the storm, over the Sao Luis station, there was an occurrence of two significant increases of hmF2 (rapid uplifts) from its mean 5QD around 13:00 and 14:00 UT, i.e., at local morning 10:00 and 11:00 LT reaching an altitude peak of 465 km and ∼520 km, respectively. The first and second rapid F-layer peak height uplifts suggest the occurrence of enhanced vertical ExB drift at the equatorial region, probably caused by PPEF episodes when $Bz < 0$ (southward) and $Ey > 0$.
- The occurrence of the two episodes of PPEF was accompanied with a significant decrease in observed MUF compared to the corrected and mean 5QD MUF values, with a deviation of about 25%. This observation implies that radio communication sectors within the equatorial and low-latitude stations can experience loss or fail of radio signal links during PPEF episodes.
- Before the ending of the geomagnetic storm's main phase, over the Sao Luis station, the F layer dynamics has a singular behavior, which is the F layer evening uplift. This F-layer evening uplift is caused by the PRE in vertical drift ExB, which results from the F-layer wind dynamo that dominates in the evening.

- On the first day of the recovery phase, at the equatorial station (Sao Luis), around local morning and noon, the Bz and Ey experienced considerable oscillations but not evident PPEF episodes were observed. Also, during the local evening of this particular day, there was no occurrence of PRE. This none occurrence of PRE is believed to be associated with DDEF.
- From the analysis of the parameters extracted from the ionograms, there was an observation of a remarkable occurrence of an additional F-layer. The observed F3 layer formed during the two episodes of PPEF that occurred in the main phase of the St Patrick's Day storm.

REFERENCES

ABDU, M.; BITTENCOURT, J.; BATISTA, I. Magnetic declination control of the equatorial f region dynamo electric field development and spread f. **Journal of Geophysical Research: Space Physics**, v. 86, n. A13, p. 11443–11446, 1981. 16

ABDU, M.; SOBRAL, J.; WALKER, G.; REDDY, B.; FEJER, B. G. Electric field versus neutral wind control of the equatorial anomaly under quiet and disturbed condition-a global perspective from sundial 86. v. 8, p. 419–430, 1990. 16, 29

ABDULLAH, S. **Observations of f-region critical frequency variation over Batu Pahat, Malaysia, during low solar activity**. PhD Thesis (PhD) — Universiti Tun Hussein Onn Malaysia, 2011. 37

ADEBESIN, B.; ADEKOYA, B.; IKUBANNI, S.; ADEBIYI, S.; ADEBESIN, O.; JOSHUA, B.; OLONADE, K. Ionospheric fof2 morphology and response of f2 layer height over jicamarca during different solar epochs and comparison with iri-2012 model. **Journal of Earth System Science**, v. 123, n. 4, p. 751–765, 2014. 35

AKASOFU, S.-I. Magnetotail phenomena during magnetospheric substorms. **Physics of magnetospheric substorms**, v. 47, p. 300–380, 1977. 6

AKASOFU, S. I. A review of the current understanding in the study of geomagnetic storms. v. 4, p. 1–13, 06 2018. 5, 6

AKASOFU, S.-I.; CHAPMAN, S. The development of the main phase of magnetic storms. **Journal of Geophysical Research**, v. 68, n. 1, p. 125–129, 1963. 6

AKASOFU, S.-I.; CHAPMAN, S.; VENKATESAN, D. The main phase of great magnetic storms. **Journal of Geophysical Research**, v. 68, n. 11, p. 3345–3350, 1963. 6

ASTAFYEVA, E.; ZAKHARENKOVA, I.; HOZUMI, K.; ALKEN, P.; COÏSSON, P.; HAIRSTON, M. R.; COLEY, W. R. Study of the equatorial and low-latitude electrodynamic and ionospheric disturbances during the 22–23 june 2015 geomagnetic storm using ground-based and spaceborne techniques. **Journal of Geophysical Research: Space Physics**, v. 123, n. 3, p. 2424–2440, 2018. 2, 14

ASTAFYEVA, E.; ZAKHARENKOVA, I.; HUBA, J.; DOORNBOS, E.; IJSSEL, J. Van den. Global ionospheric and thermospheric effects of the june 2015 geomagnetic disturbances: multi-instrumental observations and modeling. **Journal of Geophysical Research: Space Physics**, v. 122, n. 11, p. 11–716, 2017. 47

ATHIENO, R.; JAYACHANDRAN, P. Muf variability in the Arctic region: a statistical comparison with the ITU-R variability factors. **Radio Science**, v. 51, n. 8, p. 1278–1285, 2016. 1

BALAN, N.; BAILEY, G. Equatorial plasma fountain and its effects: possibility of an additional layer. **Journal of Geophysical Research: Space Physics**, v. 100, n. A11, p. 21421–21432, 1995. 18

BALAN, N.; BATISTA, I.; ABDU, M.; MACDOUGALL, J.; BAILEY, G. Physical mechanism and statistics of occurrence of an additional layer in the equatorial ionosphere. **Journal of Geophysical Research: Space Physics**, v. 103, n. A12, p. 29169–29181, 1998. 63

BALAN, N.; THAMPI, S.; LYNN, K.; OTSUKA, Y.; ALLEYNE, H.; WATANABE, S.; ABDU, M.; FEJER, B. F3 layer during penetration electric field. **Journal of Geophysical Research: Space Physics**, v. 113, n. A3, 2008. 63

BARCLAY, L. **Propagation of radiowaves**. [S.l.]: Iet, 2003. 25, 26

BATISTA, I.; PAULA, E. de; ABDU, M.; KANTOR, I. Comparative study of ionogram f2 peak height from different techniques. **Geofísica Internacional**, v. 30, n. 4, p. 249–252, 1991. 2

BENESTAD, R. E. Solar activity and regional climate variations. **Solar Activity and Earth's Climate**, p. 251–276, 2006. 3

BHASKAR, A.; VICHARE, G. Characteristics of penetration electric fields to the equatorial ionosphere during southward and northward imf turnings. **Journal of Geophysical Research: Space Physics**, v. 118, n. 7, p. 4696–4709, 2013. 5

BORA, S. Ionosphere and radio communication. **Resonance**, v. 22, n. 2, p. 123–133, 2017. 1

BYCHKOV, V. L.; GOLUBKOV, G. V.; NIKITIN, A. I. **The atmosphere and ionosphere**. [S.l.]: Springer, 2010. 1

CANCK, M. H. D. Critical frequency. 2002. Available from: <`https://ftp.unpad.ac.id/orari/library/library-sw-hw/amateur-radio/propagation/Radio%20Wave%20Propagation%20part%206%20-%20Critical%20Frequency.pdf`>. Access in: 2021. 38, 39

CANDER, L. R.; BAMFORD, R.; HICKFORD, J. Nowcasting and forecasting the fof2, muf (3000) f2 and tec based on empirical models and real-time data. In:

International conference on antennas and propagation. [s.n.], 2003. Available from: <`https://www.researchgate.net/publication/4100858_Nowcasting_and_forecasting_the_foF2_MUF3000F2_and_TEC_based_on_empirical_models_and_real-time_data`>. Access in: 2021. 1

CARRASCO, A.; BATISTA, I.; ABDU, M. The prereversal enhancement in the vertical drift for fortaleza and the sporadic e layer. **Journal of Atmospheric and Solar-Terrestrial Physics**, v. 67, n. 16, p. 1610–1617, 2005. 16

CHAPMAN, S. The electric current-systems of magnetic storms. **Terrestrial Magnetism and Atmospheric Electricity**, v. 40, n. 4, p. 349–370, 1935. 6

CHERKASHIN, Y. N.; EGOROV, I.; URYADOV, V.; PONYATOV, A. Experimental studies of variations in the maximum usable frequency on oblique sounding paths. **Radiophysics and Quantum Electronics**, v. 46, n. 12, p. 904–908, 2003. 2

CHUKWUMA, V. On geomagnetic storms and ionospheric radio wave absorption in the equatorial region: a philosophical reinforcement. In: **42nd COSPAR Scientific Assembly**. [s.n.], 2018. v. 42, p. C1–3. Available from: <`https://www.ursi.org/proceedings/procGA14/papers/ursi_paper1180.pdf`>. Access in: 2021. 22

ECCLES, W. H. On the diurnal variations of the electric waves occurring in nature, and on the propagation of electric waves round the bend of the Earth. **Proceedings of the Royal Society of London. Series A, Containing Papers of a Mathematical and Physical Character**, v. 87, n. 593, p. 79–99, 1912. 22

FAGRE, M.; ZOSSI, B. S.; YIĞIT, E.; AMIT, H.; ELIAS, A. G. Effects of earth's magnetic field variation on high frequency wave propagation in the ionosphere. **Annales Geophysicae Discussions**, p. 1–23, 2019. 25, 70

FEJER, B. G.; PAULA, E. D.; HEELIS, R.; HANSON, W. Global equatorial ionospheric vertical plasma drifts measured by the AE-E satellite. **Journal of Geophysical Research: Space Physics**, v. 100, n. A4, p. 5769–5776, 1995. 1

FEJER, B. G.; SCHERLIESS, L.; PAULA, E. D. Effects of the vertical plasma drift velocity on the generation and evolution of equatorial spread f. **Journal of Geophysical Research: Space Physics**, v. 104, n. A9, p. 19859–19869, 1999. 18

GOSLING, J.; PIZZO, V. Formation and evolution of corotating interaction regions (CIRs) and their three dimensional structure. **Corotating Interaction Regions**, p. 21–52, 1999. 47

GRODJI, F.; DOUMBIA, V.; BOKA, K.; AMORY-MAZAUDIER, C.; COHEN, Y.; FLEURY, R. Estimating some parameters of the equatorial ionosphere electrodynamics from ionosonde data in West Africa. **Advances in Space Research**, v. 59, n. 1, p. 311–325, 2017. 21

HABARULEMA, J. B.; KATAMZI, Z. T.; YIZENGAW, E. A simultaneous study of ionospheric parameters derived from FORMOSAT-3/COSMIC, GRACE, and CHAMP missions over middle, low, and equatorial latitudes: comparison with ionosonde data. **Journal of Geophysical Research: Space Physics**, v. 119, n. 9, p. 7732–7744, 2014. 2

HAIGH, J.; CARGILL, P. **The sun's influence on climate**. [S.l.]: Princeton University Press, 2015. 22

HEAVISIDE, O. Telegraphy. In: **Encyclopaedia Britanica**. [S.l.]: William Benton, 1902. p. 214. 21, 22

HOQUE, M. M.; JAKOWSKI, N. A new global model for the ionospheric f2 peak height for radio wave propagation. **Annales Geophysicae**, v. 30, n. 5, p. 797–809, 2012. 37

ILYIN, N.; BUBNOVA, T.; GROZOV, V.; PENZIN, M.; PONOMARCHUK, S. Real-time forecast of MUF for radio paths from current data obtained from oblique sounding with continuous chirp signal. **Solar-Terrestrial Physics**, v. 4, n. 3, p. 83–91, 2018. 2

IYEMORI, T.; TANAKA, Y.; TAIRA, K.; CHOQUE, E.; ROSALES, D.; MATSUMURA, M.; NAKANISHI, K.; YAMANAKA, S.; ISHITSUKA, J.; GEOMAGNETIC, B.; TEAM, H. Ionospheric and field-aligned currents caused by the lower atmospheric disturbances. In: **Abstracts**. [S.l.]: AGU Fall Meeting, 2010. v. 2010, p. SA23A–1785. 10

JORDANOVA, V. K.; ILIE, R.; CHEN, M. W. Introduction and historical background. In: **Ring concurrent investigations.** Elsevier, 2020. p. 1–13. Available from: <`https://www.elsevier.com/books/ring-current-investigations/jordanova/978-0-12-815571-4`>. Access in: 2021. 3, 4

KARAMI, K.; GHADER, S.; RAEEN, A. Comparison of peak characteristics of F2 ionospheric layer over Tehran region at a low solar activity period with IRI-2001 and IRI-2007 models predictions. **Advances in Space Research**, v. 48, n. 6, p. 1049–1055, 2011. 37

KARIM, G.; ZERBO, J. L.; KABORÉ, M.; OUATTARA, F. Critical frequency foF2 variations at Korhogo station from 1992 to 2001 prediction with IRI-2012. **International Journal of Geophysics**, v. 2019, 2019. 40

KELLEY, C. **The Earth's electric field: sources from Sun to Mud**. [S.l.]: Newnes, 2013. 12, 13

KELLEY, M. C. **The Earth's ionosphere: plasma physics and electrodynamics**. [S.l.]: Academic Press, 2009. 13, 18, 19

KENNELLY, A. E. On the elevation of the electrically-conducting strata of the Earth's atmosphere. **Electrical World and Engineer**, v. 39, n. 11, p. 473, 1902. 21, 22

KHMYROV, G. M.; GALKIN, I. A.; KOZLOV, A. V.; REINISCH, B. W.; MCELROY, J.; DOZOIS, C. Exploring digisonde ionogram data with SAO-X and DIDBase. **AIP Conference Proceedings**, v. 974, n. 1, p. 175–185, 2008. 35

KIRCHHOFF, V. W. **Introdução à geofísica espacial**. [S.l.]: Nova Stella/EDUSP/FAPESP, 1991. 1, 13

LANG, K. R. **The Cambridge encyclopedia of the Sun**. [S.l.: s.n.], 2001. 27

LIMBERGER, M. **Ionosphere modeling from GPS radio occultations and complementary data based on B-splines**. PhD Thesis (PhD) — Technische Universität München, 2015. 12

LLOSA, E. B.; ALTADILL, D.; CURTO, J. J. Ionospheric effects of the 20 november 2003 geomagnetic storm observed from gps, ground-based and satellite data. In: **Ramon Llull University/ European Geosciences Union**. [s.n.], 2007. Available from: <`https://www.fundaciongarciasineriz.es/wp-content/uploads/attachments/EBlanch_JGS.pdf`>. Access in: 2021. 70

MAEDA, K.-i. Conductivity and drifts in the ionosphere. **Journal of Atmospheric and Terrestrial Physics**, v. 39, n. 9-10, p. 1041–1053, 1977. 15

MATHIS, M. The equatorial anomaly. In: **The greatest standing errors in Physics and Mathematics**. [s.n.], 2013. Available from: <http://milesmathis.com/equat.pdf>. Access in: 2021. xv, 20

MENDILLO, M.; WROTEN, J.; ROBLE, R.; RISHBETH, H. The equatorial and low-latitude ionosphere within the context of global modeling. **Journal of atmospheric and solar-terrestrial physics**, v. 72, n. 4, p. 358–368, 2010. 2

MENVIELLE, M.; IYEMORI, T.; MARCHAUDON, A.; NOSÉ, M. Geomagnetic indices. In: **Mandea M., Korte M. (eds) Geomagnetic observations and models**. [S.l.: s.n.], 2011. p. 183–228. 8

OBROU, O.; BILITZA, D.; ADENIYI, J.; RADICELLA, S. Equatorial F2-layer peak height and correlation with vertical ion drift and M(3000)F2. **Advances in Space Research**, v. 31, n. 3, p. 513–520, 2003. 36, 37

ODRIOZOLA, S. S. **Study of plasma irregularity in the ionospheric region between E and F Layers in the Brazilian sector using rocket measurements**. Dissertation (Master in Space Geophysics) — Instituto Nacional de Pesquisas Espaciais (INPE), São José dos Campos, 2013. Available from: <http://urlib.net/8JMKD3MGP3W34P/3MHF9DS>. Access in: 2021. 30, 31

OYEKOLA, O.; FAGUNDES, P. Equatorial F2-layer variations: comparison between F2 peak parameters at Ouagadougou with the IRI-2007 model. **Earth, Planets and Space**, v. 64, n. 6, p. 553–566, 2012. 36

PIETRELLA, M.; PERRONE, L. A local ionospheric model for forecasting the critical frequency of the F2 layer during disturbed geomagnetic and ionospheric conditions. **Annales Geophysicae**, v. 26, n. 2, p. 323–334, 2008. 2, 25

RAM, S. T.; KUMAR, S.; SU, S.-Y.; VEENADHARI, B.; RAVINDRAN, S. The influence of corotating interaction region (cir) driven geomagnetic storms on the development of equatorial plasma bubbles (epbs) over wide range of longitudes. **Advances in Space Research**, v. 55, n. 2, p. 535–544, 2015. 3, 4, 5

RAM, S. T.; YOKOYAMA, T.; OTSUKA, Y.; SHIOKAWA, K.; SRIPATHI, S.; VEENADHARI, B.; HEELIS, R.; AJITH, K.; GOWTAM, V. S.; GURUBARAN, S.; SUPNITHI, M.; HUY, L. Duskside enhancement of equatorial zonal electric field response to convection electric fields during the St. Patrick's day storm on 17 March 2015. **Journal of Geophysical Research: Space Physics**, v. 121, n. 1, p. 538–548, 2016. 5

RAWER, K.; EYFRIG, R. Improving the M(3000) - hmF2 relation. **Advances in Space Research**, v. 33, n. 6, p. 878–879, 2004. 37

REINISCH, B. W.; XUEQIN, H. Automatic calculation of electron density profiles from digital ionograms: 3. processing of bottomside ionograms. **Radio Science**, v. 18, n. 3, p. 477–492, 1983. 33

RUSSELL, C. T.; KIVELSON, M. G. **Introduction to space physics**. [S.l.]: Cambridge University Press, 1995. 1, 19, 30

SANTOS, J. S. **Study of the generation of plasma bubbles under different meteorological and ionospheric conditions: observations and simulation**. Dissertation (Master in Space Geophysics) — Instituto Nacional de Pesquisas Espaciais (INPE), São José dos Campos, 2013. Available from: <http://urlib.net/8JMKD3MGP7W/3DUU2GE>. Access in: 2021. 30, 31

SAO EXPLORER. **Interactive ionogram Scaling Technologies**. 2016. Available from: <http://ulcar.uml.edu/SAO-X/SAO-X.html>. Access in: 31 Jan. 2021. 31

SCHWENN, R. Space weather: the solar perspective. **Living Reviews in Solar Physics**, v. 3, n. 1, p. 1–72, 2006. 4, 5

SHIMAZAKI, T. World-wide daily variations in the height of the maximum electron density of the ionospheric F2 layer. **Journal of the Radio Research Laboratory**, v. 2, p. 85–97, 1955. 37

SOUZA, J. R. Class note on ionospheric physics. 2019. 16, 17

SOUZA, R. J.; BATISTA, S. I.; COSTA, F. R. A simple method to calculate the Maximum Usable Frequency (MUF). In: **INTERNATIONAL CONGRESS OF THE BRAZILIAN GEOPHYSICAL SOCIETY, 13**. [S.l.]: Proceedings of EXPOGEF, Rio de Janeiro, Brazil., 2013. p. pp. 26–29. 39, 40, 42, 53, 54

TIWARI, B. R. **Atmospheric-ionospheric disturbances in the MLT region during convective climate: an integrated approach**. Thesis (Doctorate in Space Geophysics) — Instituto Nacional de Pesquisas Espaciais (INPE), São José dos Campos, 2015. Available from: <http://urlib.net/8JMKD3MGP3W34P/3KK4Q3S>. Access in: 2021. 15

VENKATESH, K.; RAM, S. T.; FAGUNDES, P.; SEEMALA, G. K.; BATISTA, I. Electrodynamic disturbances in the brazilian equatorial and low-latitude ionosphere on st. patrick's day storm of 17 march 2015. **Journal of Geophysical Research: Space Physics**, v. 122, n. 4, p. 4553–4570, 2017. 1, 5, 56, 63

VRŠNAK, B.; TEMMER, M.; VERONIG, A. M. Coronal holes and solar wind high-speed streams: Ii. forecasting the geomagnetic effects. **Solar Physics**, v. 240, n. 2, p. 331–346, 2007. 47

WOHLWEND, C. S. **Modeling the electrodynamics of the low-latitude ionosphere**. Thesis (Doctorate in Physics) — Utah State University, Utah, USA, 2008. Available from: <`https://digitalcommons.usu.edu/etd/11/`>. Access in: 2021. 1

WU, C.-C.; LIOU, K.; LEPPING, R. P.; HUTTING, L.; PLUNKETT, S.; HOWARD, R. A.; SOCKER, D. The first super geomagnetic storm of solar cycle 24:"the St. Patrick's day event (17 March 2015)". **Earth, Planets and Space**, v. 68, n. 1, p. 1–12, 2016. 44

YEERAM, T. Interplanetary drivers of daytime penetration electric field into equatorial ionosphere during CIR-induced geomagnetic storms. **Journal of Atmospheric and Solar-Terrestrial Physics**, v. 157, p. 6–15, 2017. 6

YU, Y.; WAN, W.; XIONG, B.; REN, Z.; ZHAO, B.; ZHANG, Y.; NING, B.; LIU, L. Modeling Chinese ionospheric layer parameters based on EOF analysis. **Space Weather**, v. 13, n. 5, p. 339–355, 2015. 2

ZAWDIE, K. A.; DROB, D. P.; SISKIND, D. E.; COKER, C. Calculating the absorption of hf radio waves in the ionosphere. **Radio Science**, v. 52, n. 6, p. 767–783, 2017. 23

ZHANG, M.; SHI, J.; WANG, X.; WU, S.; ZHANG, S. Comparative study of ionospheric characteristic parameters obtained by DPS-4 digisonde with IRI2000 for low latitude station in China. **Advances in Space Research**, v. 33, n. 6, p. 869–873, 2004. 2

ZHANG, M.-L.; LIU, C.; WAN, W.; LIU, L.; NING, B. Evaluation of global modeling of M(3000)F2 and hmF2 based on alternative empirical orthogonal function expansions. **Advances in Space Research**, v. 46, n. 8, p. 1024–1031, 2010. 40